remote sensing

MDPI

Article

Design and Verification of a Double-Grating Spectrometer System (DGSS) for Simultaneous Observation of Aerosols, Water Vapor and Clouds

Jifeng Li [1,2], Guanyu Lin [1,*], Heng Wu [1,2], Minzheng Duan [2,3], Diansheng Cao [1] and Longqi Wang [1]

[1] Changchun Institute of Optics, Fine Mechanics and Physics, Chinese Academy of Sciences, Changchun 130033, China; lijifeng17@mails.ucas.ac.cn (J.L.); wuheng18@mails.ucas.ac.cn (H.W.); caodiansheng@ciomp.ac.cn (D.C.); wanglongqi@ciomp.ac.cn (L.W.)
[2] University of Chinese Academy of Sciences, Beijing 100049, China; dmz@mail.iap.ac.cn
[3] Key Laboratory of Middle Atmosphere and Global Environment Observation, Institute of Atmospheric Physics, Chinese Academy of Sciences, Beijing 100029, China
* Correspondence: linguanyu@ciomp.ac.cn

Abstract: Simultaneous observation of aerosols, water vapor, and clouds is conducive to the analysis of their interactions, and the consistency of observation equipment, instrument performance, and observation time is crucial. Molecular oxygen A-band (758–778 nm) and water vapor absorption band (758–880 nm) are two bands with similar wavelengths, and the hyperspectral remote sensing information of these two bands can be exploited to invert the vertical profile of aerosol and water vapor. In this paper, a double-grating spectrometer system (DGSS) was developed. DGSS uses a telescope system and fiber to introduce multi-angle, double-band sunlight, and it splits light synchronously (non-sequentially) to different positions of the detector through a slit plate and two gratings. The DGSS was calibrated in the laboratory and observed in the external field. The results indicated that the spectral resolution reached 0.06 nm (molecular oxygen A-band, 758–778 nm) and 0.24 nm (water vapor absorption band, 758–880 nm). Meanwhile, the spectra of the two bands (three angles in each band) are not aliased on the detector. Besides, the multi-angle simultaneous observation of the high-resolution spectra of the two bands is realized, which proves the effectiveness of this method. This study will provide a scientific basis for the observation of aerosol, water vapor, and cloud ground-based networks.

Keywords: aerosol; water vapor; molecular oxygen A-band; high spectral resolution; calibration

Citation: Li, J.; Lin, G.; Wu, H.; Duan, M.; Cao, D.; Wang, L. Design and Verification of a Double-Grating Spectrometer System (DGSS) for Simultaneous Observation of Aerosols, Water Vapor and Clouds. *Remote Sens.* **2022**, *14*, 2492. https://doi.org/10.3390/rs14102492

Academic Editors: Simone Lolli, Kai Qin, Jason Blake Cohen and Davide Dionisi

Received: 14 April 2022
Accepted: 19 May 2022
Published: 23 May 2022

1. Introduction

Aerosols, water vapor, and clouds are the three main parameters that affect global climate change and the atmospheric energy cycle [1–3]. Through the long-term accumulation of the spatial and temporal distribution of the three parameters, it is possible to better predict and evaluate the impact of human activities on global changes [1,4,5]. Furthermore, it is possible to discover how to change production methods to better adapt to and regulate the trend of climate change [4–6]. Remote sensing technology (including ground-based, sky-based, and space-based) is the main method for obtaining long-term observational data of aerosols, water vapor, and clouds.

Aerosols affect the global energy radiation balance in two ways [5,7–11]. The first is the direct scattering of solar radiation [12]. The second is the condensation nucleus of the cloud in the process of cloud formation, evolution, and dissipation [3,13–15], which changes the microphysical structure, life span, and optical properties of the cloud [16], thereby affecting the global radiation budget [1,2,5,13]. The vertical profile is a very important parameter for understanding aerosols [17]. The methods for observing the vertical profile of aerosols have some limitations. Firstly, the observation of a high tower can only be

carried out near the ground due to the height problem. Meanwhile, due to the condensation of water vapor, coupled with the problem of a high maintenance cost, a large range of laser observations cannot be conducted. Besides, aircraft telemetry can only be used for short-term observation and cannot reflect the aerosol parameters in a specific area for a long time. In addition, satellite remote sensing, greatly affected by weather, cannot achieve all-weather observations [18–21]. Therefore, low-cost remote sensing instruments suitable for observing vertical profiles of aerosols in the observation station network are very important.

Water vapor and clouds (liquid phase and ice phase) are the two forms of water, and the conversion between water vapor, liquid water, and ice is an important part of the energy conversion of the earth-atmosphere system [7,22–26]. With global warming, the tropospheric water vapor content increases [27–29], and the total amount of precipitable water stored in the atmosphere increases [2,22,30]. Driven by the atmospheric circulation, the regional distribution of water indicates an increase in the probability of extreme floods and disasters in some areas [29,31–33], and it leads to the frequent occurrence of extreme drought events in other areas [22]. The remote sensing inversion of water vapor and cloud parameters is an important data source for revealing the atmospheric water cycle [26], which helps to accurately evaluate the conversion process of water between the atmosphere and the surface and improve the accuracy and prediction effectiveness of the existing climate models. In terms of water vapor detection, the main detection methods at present include the infrared remote sensing method, differential laser method, Raman laser method, microwave radiometer method, and GPS method. Infrared remote sensing can only be performed under cloudless weather conditions and cannot identify cloud phases. Laser methods and microwave detection methods are expensive. GPS water vapor detection method uses atmospheric parameters such as water vapor to invert and correlate the delay or refraction of GPS electromagnetic wave propagation. The current GPS water vapor detection method can only obtain one water vapor parameter and cannot identify cloud parameters such as cloud phases [26–28]. Therefore, it is significant to use high-resolution spectroscopic observations in the near-infrared band to extract atmospheric water vapor data on a regional scale.

Most of the research on the interaction of aerosols, water vapor, and clouds focuses on the relationship between the total amount of aerosols and cloud parameters [15,34]. However, the most significant interaction between aerosols, water vapor, and clouds is located at the cloud layer [13], and the result is very uncertain [14]. As the existing double grating spectrometers are in the way of sequential light splitting (similar to monochromator), it is difficult to realize the synchronous detection of two bands in the same instrument. In addition, as the data of different atmospheric elements are obtained from different detection equipment, there are deficiencies in the consistency of instrument performance, observation modalities, and time. Therefore, the simultaneous observation and inversion of aerosol, water vapor, and cloud parameters are particularly important.

Molecular oxygen is a uniformly mixed gas in the atmosphere. Its volume percentage is constant [35], and the absorption of other gases except for molecular oxygen in the 758–778 nm band (molecular oxygen A-band) can be completely ignored [36–38]. In this band, the absorption optical thickness of molecular oxygen ranges from zero to ten, and the dynamic range has several orders of magnitude [39]. In the high-absorption band, the surface observations and satellite observations mainly reflect the information of the upper atmosphere; in the low-absorption band, since photons can directly penetrate to the bottom of the atmosphere, the observation signals mainly come from the atmosphere or the lower layers of the clouds. Therefore, the use of multispectral data in this band can distinguish the contribution of the ground and the atmosphere at each level, thereby extracting the vertical profile of different height distributions [40–42]. The absorption of the water vapor band at 820 nm is very pure, and the absorption dynamic range is conducive to ground-based water vapor remote sensing under high spectral resolution. In this band, the same detector can be used with the molecular oxygen A-band, which is conducive to the synchronous

observation of the parameters of aerosol, water vapor, and clouds to analyze the interaction between them.

This paper aims to provide a new method to observe molecular oxygen A-band (758–778 nm) and water vapor band (758–880 nm) with double-bands, multi-angles, and high spectral resolution. Meanwhile, it provides ideas for realizing the comprehensive inversion of aerosol, water vapor, and cloud. Through the thermal analysis and design of the instrument, the problem of spectral drift in the field of long-span spectral instrument is overcome. The calibration method of hyperspectral resolution instrument is provided, which provides a new idea for the design and calibration of atmospheric detection instrument. The new method will facilitate the prediction of global climate change trends and provide a scientific basis for human intervention and adjustment of global change trends [43].

This paper is organized as follows. In Section 2, the theoretical basis (including the principle of spectral calibration and radiation calibration and the advantages of multi-angle detection), the composition, the working principle, and the thermal simulation analysis of the double-grating spectrometer system (DGSS) are introduced. Section 3 presents the calibration results of the instrument, the important technical parameters, and the measured results of the field atmosphere, which verifies the feasibility of the observation method. The experimental results are discussed in Section 4. Finally, in Section 5, the conclusions and the future work are given.

2. Materials and Methods

2.1. Theory

2.1.1. Spectral Calibration Principle

Spectral calibration of remote sensing instruments is mainly to obtain the spectral response function of each pixel on the detector, and determine the central wavelength distribution, spectral resolution and spectral range of the instrument. The central wavelength is the position corresponding to the peak of the spectral response function. The spectral resolution is the band width corresponding to the 50% peak of the spectral response function, which is also called FWHM (Full-Width Half-Maximum). Figure 1 shows the principle of the spectral response function. The ordinate represents the normalized spectral response of the detector, and the abscissa represents the wavelength [44].

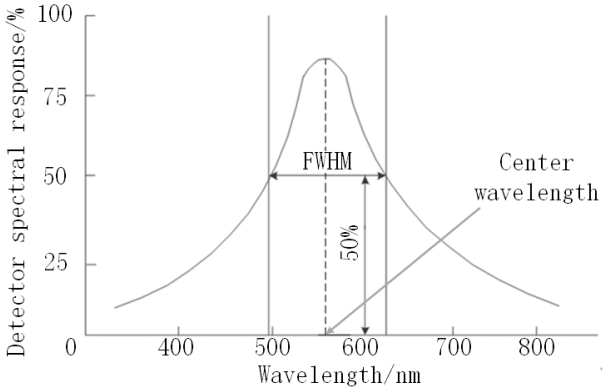

Figure 1. The principle of the spectral response function.

For general spectrometers, the wavelength and column pixel number can be fitted by a polynomial. As an example, the principle of the first-order polynomial fitting is introduced. For the pixel in row i of the detector image plane, the first-order linear regression model can be established for the wavelength λ and the pixel number m:

$$\begin{gathered} \lambda_{im}(X_{im}) = aX_{im} + b + \varepsilon \\ E(\varepsilon) = 0, D(\varepsilon) = \sigma^2 \end{gathered} \quad (1)$$

In Equation (1), a and b are regression coefficients, and X_{im} is regression variable. Assuming there are n groups of data ($m = 1, 2, 3, 4 \ldots n$), then:

$$\begin{array}{c} \lambda_{im}(X_{im}) = aX_{im} + b + \varepsilon_m \\ E(\varepsilon_m) = 0, D(\varepsilon_m) = \sigma^2 \end{array} \tag{2}$$

In Equation (2), $\varepsilon_1, \varepsilon_2, \ldots, \varepsilon_n$ are independent of each other, and the regression coefficients a and b satisfy the following relationship:

$$Q(b, a) = \sum_{m=1}^{m=n} \varepsilon_m^2 = \sum_{m=1}^{m=n} (\lambda_{im}(X_{im}) - aX_{im} - b)^2 \tag{3}$$

The estimated values $\hat{a}$ and $\hat{b}$ of regression coefficients a and b satisfy the following relationship:

$$Q(\hat{b}, \hat{a}) = \min_{b,a} Q(b, a) \tag{4}$$

The derivation of Equation (4) shows that:

$$\begin{cases} n\hat{b} + \hat{a} \sum\limits_{m=1}^{m=n} X_{im} = \sum\limits_{m=1}^{m=n} \lambda_{im} \\ \hat{b} \sum\limits_{m=1}^{m=n} X_{im} + \hat{a} \sum\limits_{m=1}^{m=n} X_{im}^2 = \sum\limits_{m=1}^{m=n} \lambda_{im} X_{im} \end{cases} \tag{5}$$

Solve Equation (5) to obtain:

$$\begin{cases} a = \dfrac{\sum\limits_{m=1}^{n} (X_{im} - \overline{X}_i)(\lambda_{im} - \overline{\lambda}_i)}{\sum\limits_{m=1}^{n} (X_{im} - \overline{X}_i)^2} \\ b = \overline{\lambda}_i - a\overline{X}_i \\ \overline{\lambda}_i = \frac{1}{n} \sum\limits_{m=1}^{m=n} \lambda_{im} \\ \overline{X}_i = \frac{1}{n} \sum\limits_{m=1}^{m=n} X_{im} \end{cases} \tag{6}$$

The correlation coefficient is calculated as:

$$R^2 = \frac{\sum\limits_{m=1}^{n} (\hat{\lambda}_{im} - \overline{\lambda}_i)^2}{\sum\limits_{m=1}^{n} (\lambda_{im} - \overline{\lambda}_i)^2} \tag{7}$$

The value range of Equation (7) is $[0, 1]$. The degree that R^2 is close to 1 reflects the fitting effect between the central wavelength and the corresponding column pixel number. Higher-order polynomial fitting is similar to the above principle.

2.1.2. Radiometric Calibration Principle

In this paper, the integrating sphere is selected as the light source for radiometric calibration. It is characterized by large output energy, good surface uniformity, and Lambertian characteristics [45]. It calibrates full aperture, full field of view, and full band at different points in the dynamic range of remote sensing instruments. Assuming that the radiance from the target scene received by the remote sensing instrument in its instantaneous field of view is L, under the ideal condition that all imaging links are linear systems, its output digital number (DN) value can be expressed as:

$$DN - DN_0 = L \cdot \frac{\pi}{4} \cdot \left(\frac{D}{f'}\right)^2 \tau_O \cdot R_D \cdot \beta_E \cdot t_{Int} \cdot A_d \tag{8}$$

In Equation (8), D/f' is the relative aperture of the optical system; τ_O is the total transmittance of the optical system including the filter; R_D is the responsiveness of the focal plane detector; β_E is the gain of the electronic system; t_{Int} is the integration time; A_d is the photosensitive surface area of a single pixel of the detector, and DN_0 is the gray output of the dark signal.

As shown in Figure 2, the integrating sphere radiometric calibration system first calibrates the radiance response of the spectral radiometer, then calibrates the spectral radiance of the integrating sphere light source with the spectral radiometer, and finally calibrates the radiance response of the remote sensing instrument. The essence of radiometric calibration is to obtain the radiation response R_i, bias b_i, and the corresponding radiation parameters of each pixel i of the remote sensing instrument according to the DN value of the obtained image and the radiance of the integrating sphere:

$$DN_i = R_i L + b_i \tag{9}$$

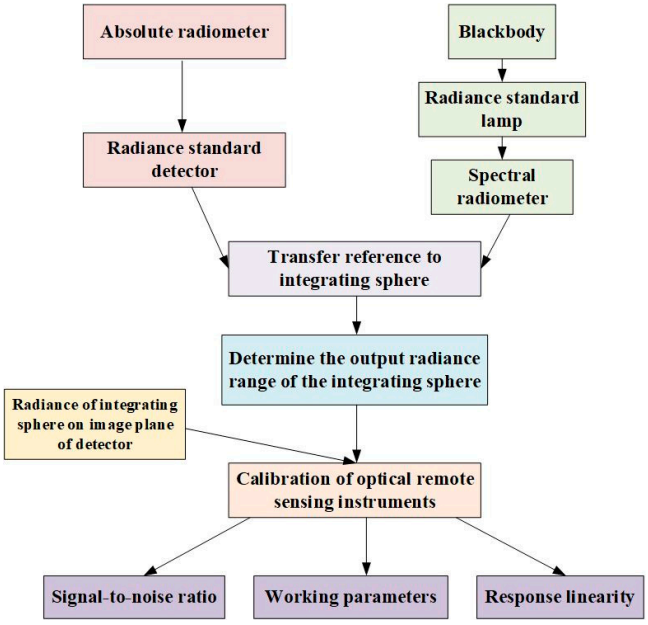

Figure 2. Transmission of radiation standards.

The integrating sphere light source is used to simulate the actual observation target for image acquisition. The ratio of the statistical average gray value of each pixel of the remote sensing instrument is calculated row by row to obtain the statistical root mean square noise, that is, the signal-to-noise ratio (SNR) of the pixel under this lighting condition:

$$SNR = \frac{\overline{DN}}{\sqrt{\frac{\sum_{i=1}^{N} (DN_i - \overline{DN})^2}{N-1}}} \tag{10}$$

Equation (10) shows the SNR analyzed from the perspective of radiometric calibration. From the perspective of the detector, the SNR can be expressed as:

$$SNR = \frac{S_e}{\sqrt{S_e + n_{dark} + {\sigma_{read}}^2}} \tag{11}$$

In Equation (11), S_e is the number of target signal electrons, n_{dark} is the number of dark current electrons, and σ_{read} is the readout noise. The light energy received by a pixel

on the detector is the product of image plane illumination, pixel area, and integration time. The number of signal electrons S_e generated by target radiation can be expressed as:

$$S_e = [\int_{\lambda}^{\lambda+\Delta\lambda} E'(\lambda) A_d t_{\text{int}} \eta(\lambda) d\lambda] / (hc/\lambda) \tag{12}$$

In Equation (12), $E'(\lambda)$ is the spectral irradiance of the image plane; A_d is the area of the detector pixel; t_{int} is the integration time; $\eta(\lambda)$ is the quantum efficiency of the detector; $h = 6.63 \times 10^{-34}$ J·s is the Planck constant; $c = 3 \times 10^8$ m/s is the speed of light, and λ is the wavelength. Image plane spectral irradiance $E'(\lambda)$ can be expressed as:

$$E'(\lambda) = L(\lambda)\tau_o(\lambda)\frac{\pi}{4}\left(\frac{D}{f}\right)^2 \tag{13}$$

In Equation (13), $L(\lambda)$ is the spectral radiance received by the instrument, $\tau_o(\lambda)$ is the spectral radiation transmission efficiency of the optical system, and D/f is the relative aperture of the optical system. Substitute Equation (13) into Equation (12) to obtain:

$$S_e = \frac{\pi A_d t_{\text{int}} \lambda}{4hc}\left(\frac{D}{f}\right)^2 \int_{\lambda}^{\lambda+\Delta\lambda} L(\lambda)\tau_o(\lambda)\eta(\lambda)d\lambda \tag{14}$$

To obtain a high spectral resolution (0.07 nm), the slit of DGSS is only 25 μm. This will cause the signal received by the instrument to be weak and the SNR to be reduced. In this paper, the back-illuminated detector with high quantum efficiency is selected, and the spatial pixel combination is conducted to improve the SNR.

2.1.3. Advantages of Multi-Angle Detection

Multi-angle detection can provide more independent information [46–49]. To analyze the advantages of multi-angle detection, it is assumed that the vertical distribution of aerosol and water vapor is exponentially decreasing, and the "elevation" parameter is used to indicate the difference between different profiles. Figure 3 shows the difference between single-angle and multi-angle inversion of aerosol and water vapor. It can be seen that multi-angle detection inversion can effectively reduce the inversion error of aerosol and water vapor in both total and profile inversion.

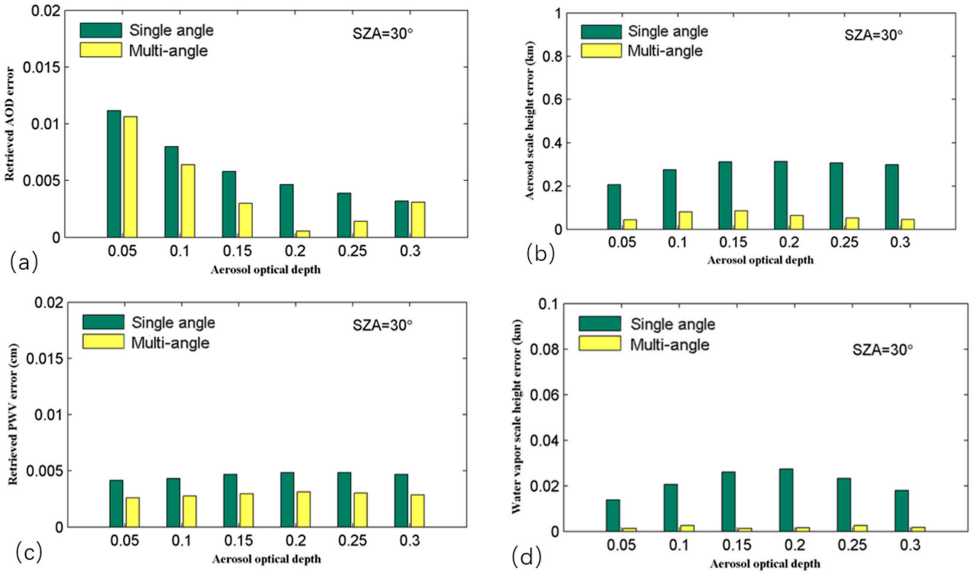

Figure 3. Comparison of single-angle and multi-angle inversion errors (AOD: Aerosol Optical Depth, PWV: Precipitable Water Vapor, SZA: Solar Zenith Angle): (**a**) Aerosol optical depth error; (**b**) Aerosol scale height error; (**c**) Retrieved PWV error; (**d**) Water vapor scale height error.

2.2. Instrument Design

In order to achieve simultaneous observation of the molecular oxygen A-band (758–778 nm) and the water vapor band (758–880 nm) and to achieve simultaneous inversion of aerosol, water vapor, and cloud-related parameters, DGSS needs to collect the spectral information of the two bands with the same detector at the same time without spectral aliasing. Meanwhile, to obtain the vertical profile information of aerosol and water vapor, DGSS needs to have extremely high spectral resolution and an excellent ability to restrain stray light. Besides, to effectively reduce aerosol and water vapor for the inversion error, it is necessary to introduce multiple angles of light into the DGSS. In addition, DGSS needs to experience different temperature environments in field experiments, so the stability of DGSS at different temperatures is also important.

2.2.1. Instrument Composition

As shown in Figure 4, DGSS is composed of a multi-angle front telescope system, a solar tracking turntable, a double-grating spectrometer, and a program control computer.

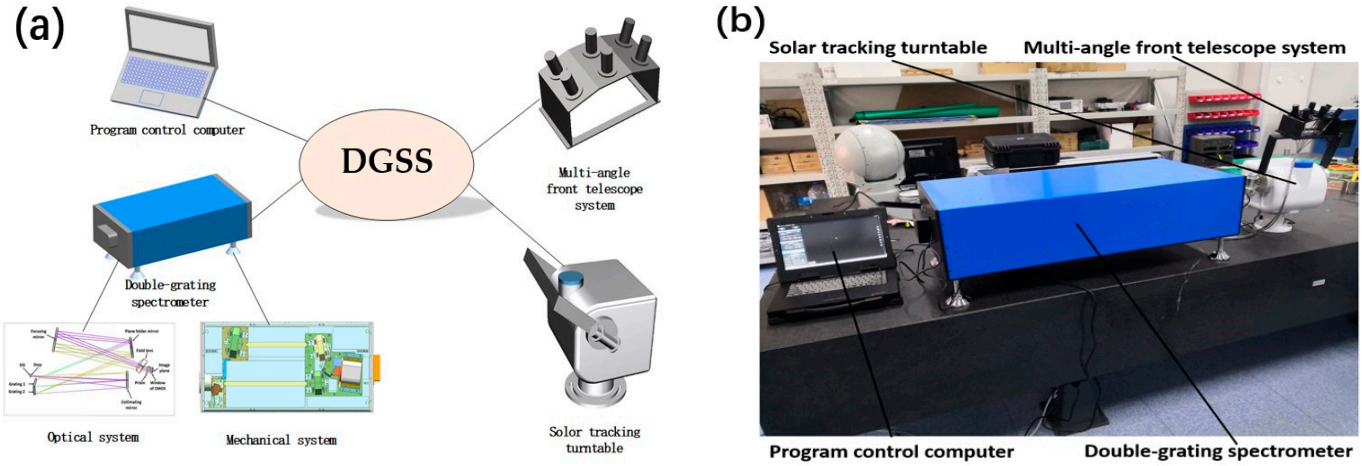

Figure 4. The components of DGSS: (**a**) Schematic diagram; (**b**) Physical diagram.

The multi-angle front telescope system consists of six telescopes. A narrow-band filter is installed at the front end of the telescope to suppress out-of-band radiation. Its transmittance curve is shown in Figure 5. The telescope has a focal length of 22.92 mm, a field of view of 1.5°, and an F-number of 2.27. The optical structure of the telescope system is shown in Figure 6. Among the six telescopes, two are direct solar channels, four are sky scattering channels, and the scattering channels and direct channels are arranged on the support frame at 15° and 37.5°, respectively (the angle can be changed by changing the installation method). The support frame needs to ensure good position accuracy and cooperate with the interface of the sun tracking turntable. The position relationship of the telescope is shown in Figure 7.

The solar tracking turntable carries six multi-angle telescopes and a four-quadrant detector, as shown in Figure 8. The turntable has a good mass and inertia distribution to ensure the best dynamic stiffness characteristics and reduce the interference to the DGSS spectrum line during the tracking process. Furthermore, it has sufficient strength and rigidity to ensure that the structure has no plastic deformation under the specified mechanical conditions and does not affect the sun-tracking accuracy. Besides, the turntable has good temperature adaptability to ensure that the mechanism works normally within the working temperature range. In addition, it also has stable size and accuracy within the design temperature range (−25~45 °C).

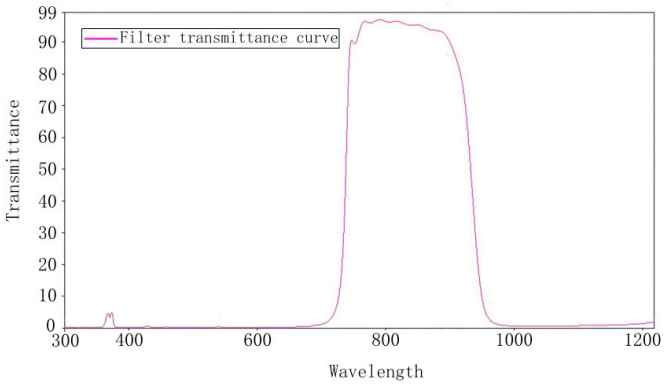

Figure 5. The transmittance curve of the narrow-band filter at the front end of the telescope.

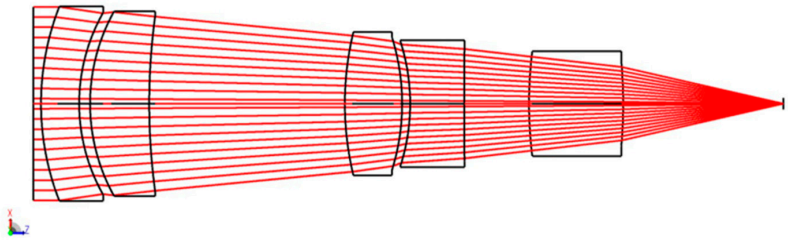

Figure 6. The internal optical structure of a single tube of the multi-angle front telescope.

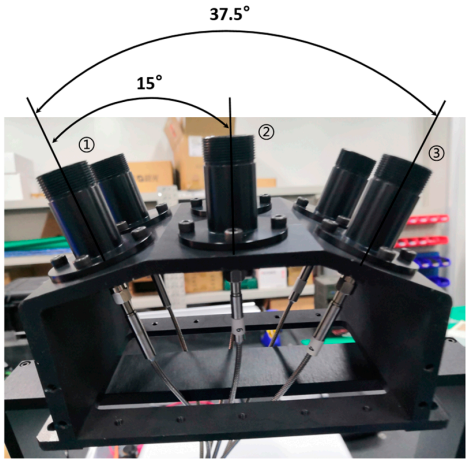

Figure 7. The positional relationship between six multi-angle front telescopes (The position of ① in the figure corresponds to two direct solar channels, and the positions of ② and ③ correspond to four sky scattering channels).

The double-grating spectrometer is composed of an outer shell, a frame, a supporting part, a connecting part, an adjustment part, a slit piece, a stop, a collimator lens, a double-grating, a plane folding mirror, a focusing lens, a field lens, and a detector. The slit piece is made of monocrystalline silicon and processed by dry particle beam etching. The two slits are staggered. The stop is made of invar material with a very small thermal expansion coefficient. The six light holes on the stop are processed by EDM (Electrical Discharge Machining) technology, and they are staggered in the X and Y directions. All the internal mirrors are coated to ensure high reflectivity while reducing the influence of stray light outside the target band. The mechanical structure and the actual internal structure of the double-grating spectrometer are shown in Figure 9a,b, respectively.

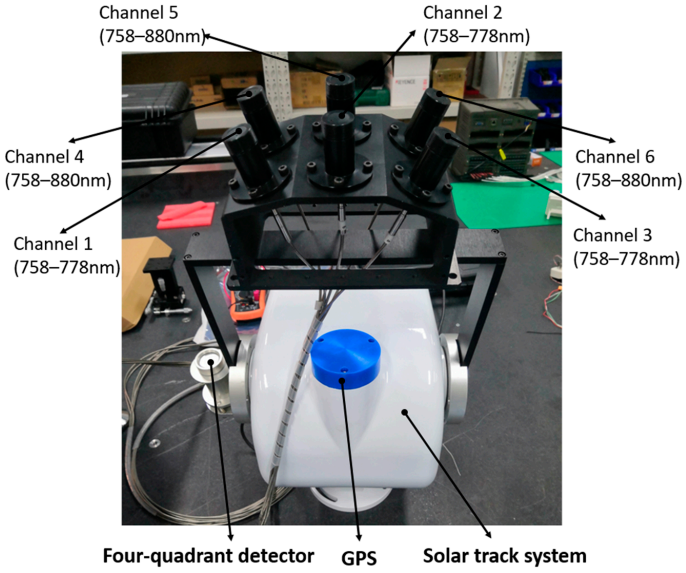

Figure 8. Several important parts of the sun tracking turntable and the installation relationship with the multi-angle front telescope.

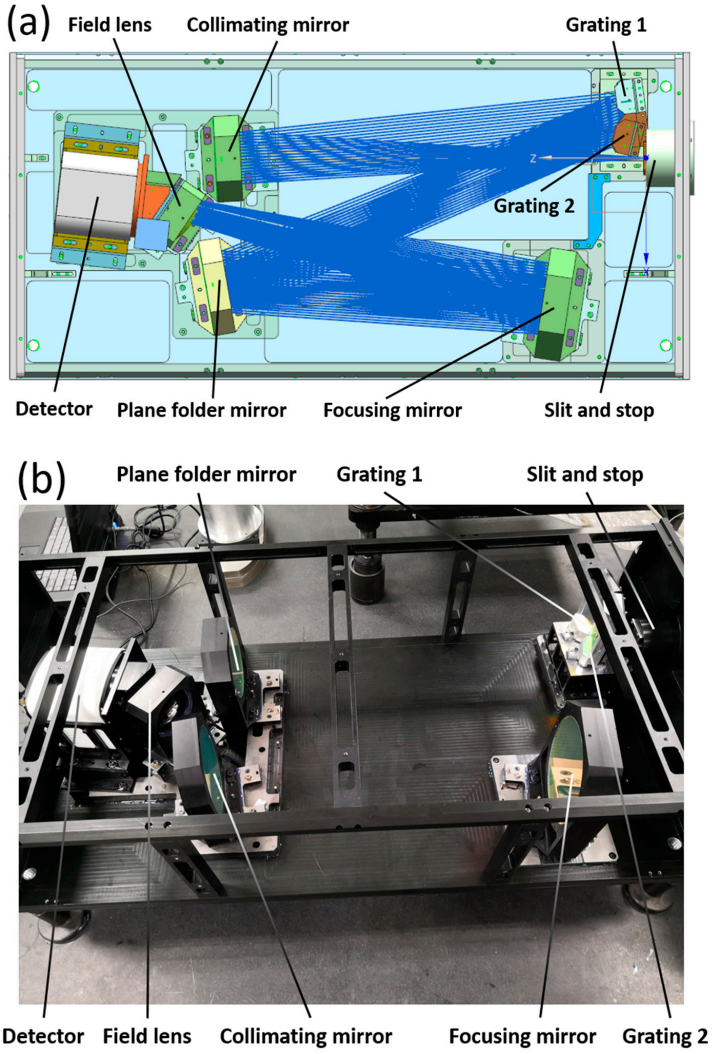

Figure 9. (**a**) The mechanical structure of the double-grating spectrometer in the design stage; (**b**) The actual internal structure of the double-grating spectrometer in the setup stage.

The double-grating spectrometer chooses a GSENSE400BSI CMOS back-illuminated detector, with a pixel size of 11 μm × 11 μm, a pixel number of 2048 × 2048, an ultra-low readout noise of 1.2e, and a dark current of only 0.2e-/s/pix@-50 °C. The CMOS is packaged with semiconductor cooling and air-cooling devices to keep the temperature around −10 °C, and the dark current is 1.5e-/pixel/s (−10 °C). Figure 10 shows the relationship between the quantum efficiency of the detector and the wavelength. It can be seen from Equations (11) and (14) in Section 2.1.2 that a lower dark current and a higher quantum efficiency are conducive to improving SNR. However, dispersive hyperspectral visible and near-infrared (VNIR) imagers using back-illuminated detectors will suffer from interference fringes in near-infrared bands [50]. If the spectral position is relatively stable on the detector image plane, the influence of interference fringes can be weakened through calibration on the premise that the actual observation conditions can be well simulated during calibration.

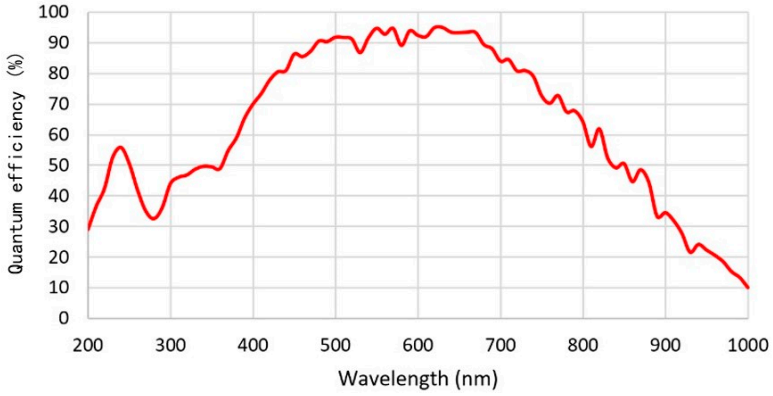

Figure 10. The relationship between the quantum efficiency of the detector and the wavelength.

The computer used for program control is an industrial customized computer that supports image acquisition, data analysis and storage, and data pre-processing. Furthermore, it is equipped with self-developed acquisition control software, so it can not only collect and store images but also has the functions of playback, zooming, pixel merging, mode change, and adjustment of integration time, thus fully meeting the needs of all aspects of the instrument use.

2.2.2. Working Principle

Next, the working principle of DGSS along the trajectory of light will be described. As shown in Figure 11, the tracking program of the solar tracking turntable uses the GPS module to input the local longitude, latitude, time, and other parameters to calculate the altitude and azimuth of the sun. Meanwhile, the sun angle information is output to the driver of the turntable to complete the initial tracking of the sun's azimuth by the turntable. Then, the closed-loop control part of the image feedback uses the four-quadrant detector to collect the current sun image. After the image of the sun is processed, the deviation of the sun track tracking is obtained. Next, this deviation is exploited to correct the sun's azimuth and the accuracy of the detection and tracking system to achieve precise tracking of the sun's azimuth, and the tracking accuracy is higher than 0.1°. After the direct channel is aligned with the sun, six multi-angle front telescopes (two are direct sun channels and four are sky scattering channels) converge the light onto the optical fiber. One end of the optical fiber is connected to the telescope tube, and the other end is connected to the slit of the spectrometer [51].

As shown in Figure 12, the size and position of the spectrometer slit and stop are designed to ensure that the six beams of light entering the system do not have spectral aliasing. The two slits are 0.6 mm away from the center in the horizontal direction and 10 mm from the center in the vertical direction. Six optical fibers are input through the slit. The upper three fibers correspond to three angles of incident light in the 758–880 nm band,

and the lower three fibers correspond to three angles of incident light in the 758–778 nm band. At a distance of 3.34 mm from the slit, a stop is placed to eliminate stray light. To prevent spectral aliasing, the stop separates the light passing through the slit in the vertical direction and blocks half of it in the horizontal direction.

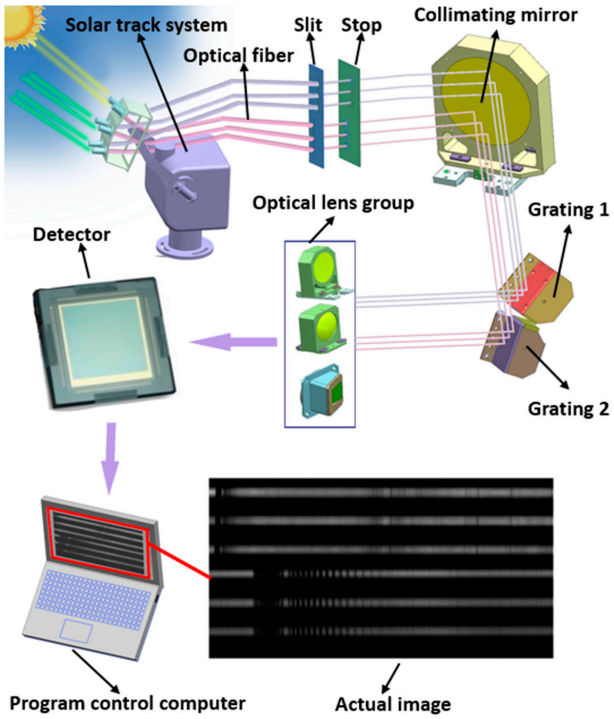

Figure 11. The working principle of DGSS along the light trail.

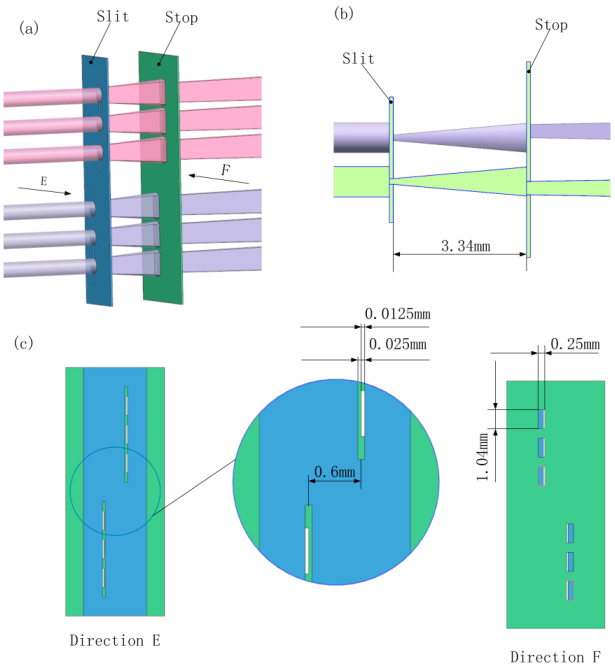

Figure 12. The positional relationship between the slit and the stop, which is one of the key factors to ensure that the spectrum does not alias on the image plane of the detector: (**a**) Schematic diagram of location relationship; (**b**) Schematic diagram of distance relationship; (**c**) Schematic diagram of dimensional relationship.

The six beams of light pass through the slit and the stop and the collimator lens and then, respectively, reach two gratings (where the light in the 758–880 nm band reaches grating 1, and the light in the 758–778 nm band reaches grating 2). Besides, both grating 1 and grating 2 work at level-1, and the stray light of other levels is suppressed by setting light barriers and absorption wells. The light split by the grating is finally converged on the image surface of the detector through the optical mirror group, and the atmospheric optical spectrum diagram processed by the program-controlled computer is displayed.

2.3. Thermal Simulation

In the traditional spectrometer, the lens holder and the bottom plate are usually installed in a fixed connection mode. When used in an environment with little temperature change, the measurement of the spectrometer is not greatly affected. However, DGSS is usually operated outdoor and tested in a large temperature range (−20 °C~40 °C), and the double-grating spectrometer has a large span in the length direction (that is, the optical path direction). If the traditional structure is adopted, when the temperature changes greatly, the deformation of the bottom plate will cause a relative position change between the optical devices and cause the shift of the spectral line position, resulting in a decrease in the accuracy of the atmospheric parameter inversion. To solve the above problems, the structure design of the double-grating spectrometer mainly suppresses the deformation caused by temperature changes from two aspects: (1) The Invar material with a small thermal expansion coefficient (the thermal expansion coefficient is 0.3 × 10–6/°C) is used to connect the main lens holders; (2) between the main lens holders, one end is fixed, and the other end is rolling support to reduce the relative distance change between the optical devices. The support method is shown in Figure 13.

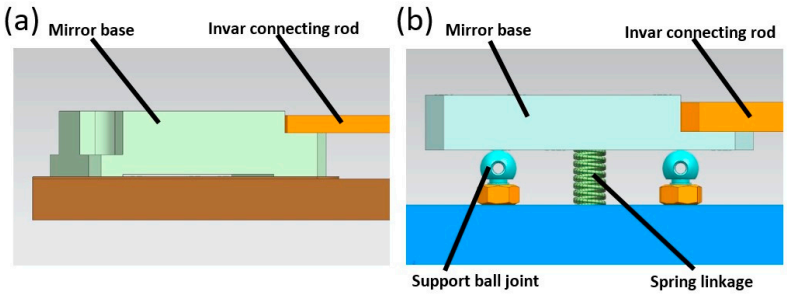

Figure 13. (**a**) Fixed support model; (**b**) Rolling support model.

For spectroscopy instruments, the stable positional relationship between the key optical components is an important factor to ensure imaging quality. Invar material is a material with a small coefficient of thermal expansion. However, due to its high density, large-area use of this material will result in high instrument mass. Therefore, this paper chooses to use this material in the connection part between each lens group. In this way, the stability of the positional relationship between the key optical devices can be ensured, and the components will not be too heavy for transportation. In the selection of the support method, temperature simulations were carried out for two methods: (1) fixed support at both ends; (2) fixed support at one end, and rolling support at the other end. The results are shown in Figure 14.

The temperature of the instrument is 20 °C when the instrument is installed and adjusted. It can be seen from the simulation results that the method of fixed support at one end and rolled support at the other end is better than that of fixed support at both ends. For a temperature change of 40 °C, the maximum deformation is only 0.14 mm, which is within the allowable tolerance (0.2 mm) of the instrument design. The drift of the spectrum can be well corrected by laser calibration.

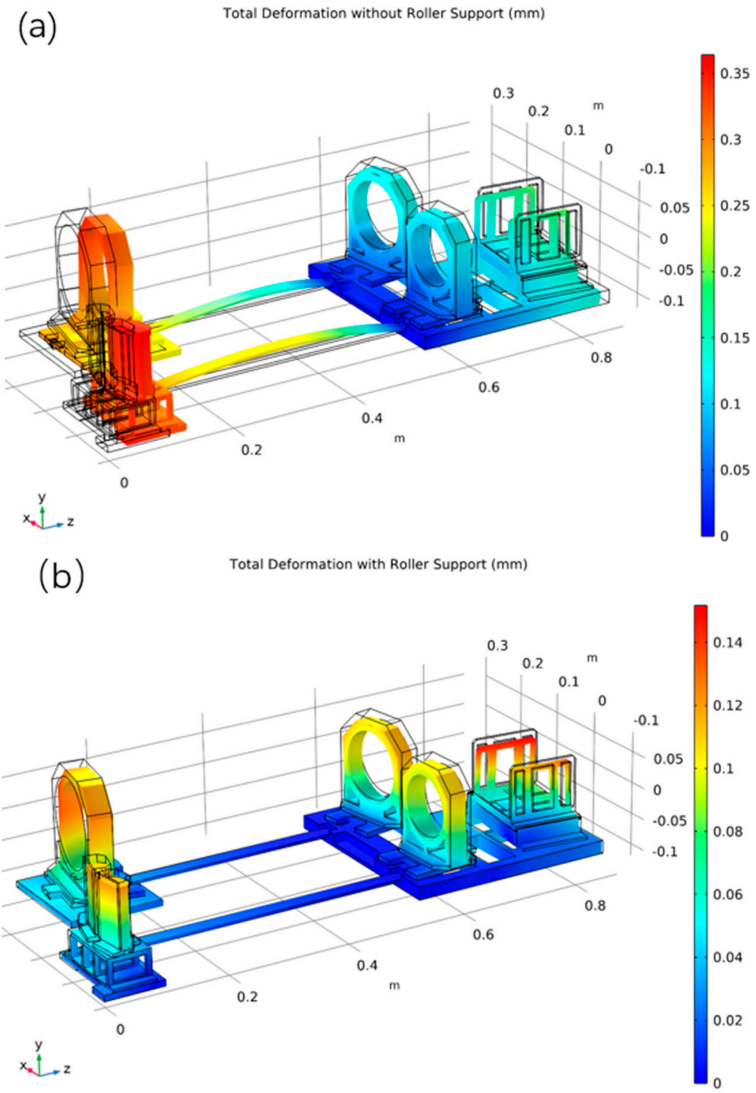

Figure 14. Comparison of thermal simulation results of the two support methods (the initial temperature is 20 °C, and the temperature change is 40 °C): (**a**) Fixed support at both ends; (**b**) Fixed support at one end and rolled support at the other end.

3. Results

3.1. Instrument Calibration

The calibration of optical remote sensing instruments includes spectral calibration and radiometric calibration. Spectral calibration obtains the spectral response function of the instrument by illuminating the instrument with monochromatic light of known wavelength and then obtains the spectral resolution and central wavelength distribution. Radiometric calibration establishes the relationship between the output of the instrument and the radiation of the detected target through the light source illumination instrument with known radiance, and obtains the response linearity, SNR, and radiation response of the instrument.

3.1.1. Spectral Calibration

According to the design of DGSS, the spectral radiance will be detected by different detector channels. In practical applications and inversion, the relationship between spectral radiance and wavelength λ needs to be obtained [52]. Thus, the DGSS must be calibrated.

In the spectral calibration process, the DGSS will be irradiated by approximately monochromatic light, with a known center wavelength, that simulates the actual observa-

tion situation. By analyzing the results of the spectral calibration, the response of every pixel on the image plane to monochromatic radiation can be obtained [53]. The central wavelength and the spectral resolution of each pixel on the image plane of the DGSS can also be obtained through Gaussian fitting of the response of every pixel.

When the light enters the DGSS, it passes through the fiber coupling, so the different positions of the spatial dimension on the image plane do not correspond to different fields of view. Meanwhile, merging the spatial dimensions is beneficial to improving the SNR of the data, so DGSS also bins the spatial dimensions during the observation period. After binning, it is redundant to discuss the response and working conditions of each pixel separately. Therefore, instead of discussing individual pixels, the subsequent discussion in this article will focus on the spectral channels (Pixel Binning Spectral Channel: PBSC) obtained after spatial dimension merging.

DGSS uses a common optical path, double-grating, and a common detector to simultaneously observe six channels in the water vapor band and the molecular oxygen A-band. This special optical design is also the starting point for the spectrum calibration experiment design. According to different observation bands, the six channels can be divided into two groups, and the design parameters are listed in Table 1. The experiment will calibrate the two observation channel gropes of the molecular oxygen A-band (758–778 nm) and the water vapor absorption band (758–880 nm).

Table 1. Comparison of the design parameters of observation channel between water vapor absorption band and molecular oxygen A-band.

Design Specifications	Observation Channel of Water Vapor Absorption Band	Observation Channel of Molecular Oxygen A-Band
Number of channels	3	3
Observation band (nm)	758–880	758–778
Spectral resolution (nm)	<0.28	<0.07

Due to the high spectral resolution of the observation channels (better than 0.07 nm) of the molecular oxygen A-band (758–778 nm), a calibration scheme combining a tunable laser and a high-sensitivity wavelength meter was used for calibration. The schematic diagram and physical diagram of the calibration system are shown in Figure 15.

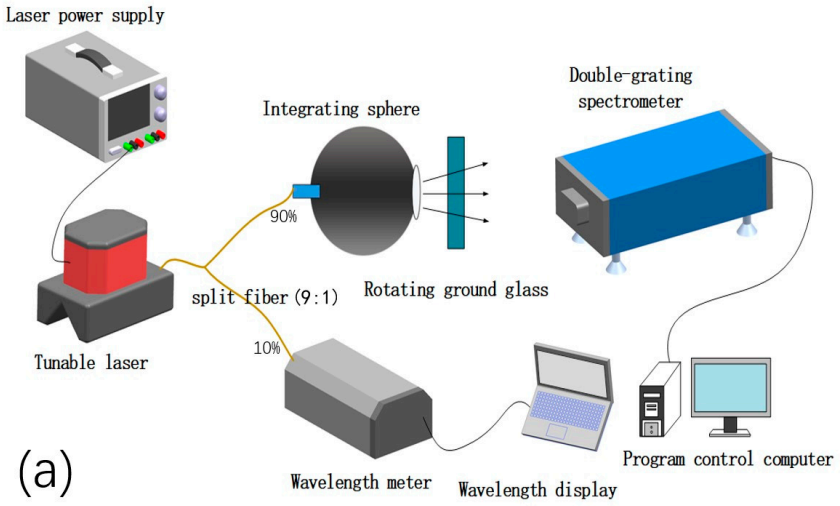

Figure 15. *Cont.*

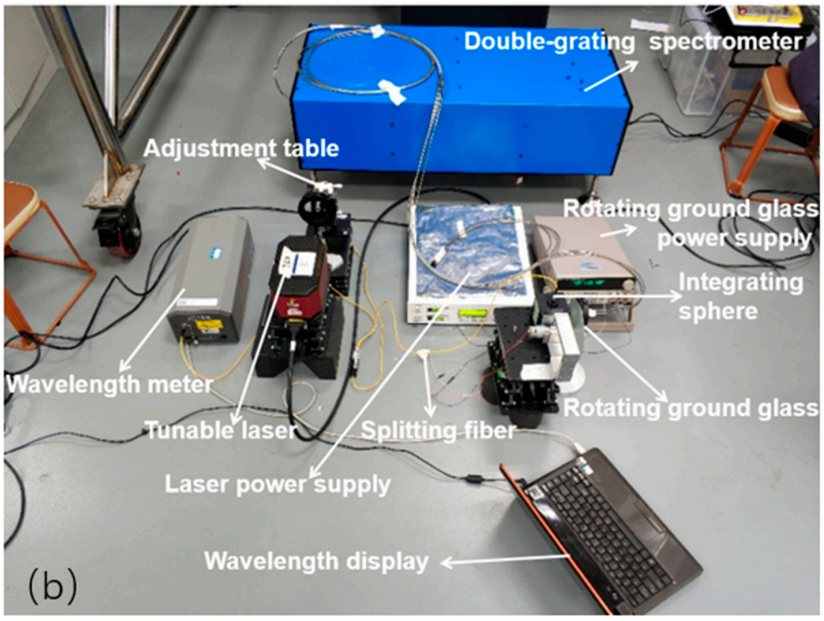

Figure 15. Molecular oxygen A-band (758–778 nm) spectrum calibration system (**a**) Molecular oxygen A-band (758–778 nm) spectrum calibration flow chart; (**b**) The instrument of the Molecular oxygen A-band (758–778 nm) spectrum calibration system and the working principle.

Under the spectral calibration demand of the water vapor band channels, the tunable laser cannot output such a wide-band (758–880 nm) radiation, so a spectrum calibration scheme combining a continuous spectrum laser and a monochromator was adopted for water vapor band channels. The schematic diagram and the physical composition of the calibration system are shown in Figure 16.

During the calibration, the tunable laser (when calibrating the molecular oxygen A-band) and the monochromator (when calibrating the water vapor absorption band) were adjusted to scan the wavelength at a certain interval. Meanwhile, the response of DGSS was recorded, that is, the instrument is in the gray value response under different monochromatic light irradiation. After the response value is processed by pixel merging, the power correction, the normalization and normal fitting, and the normalized spectral response function of each PBSC can be obtained.

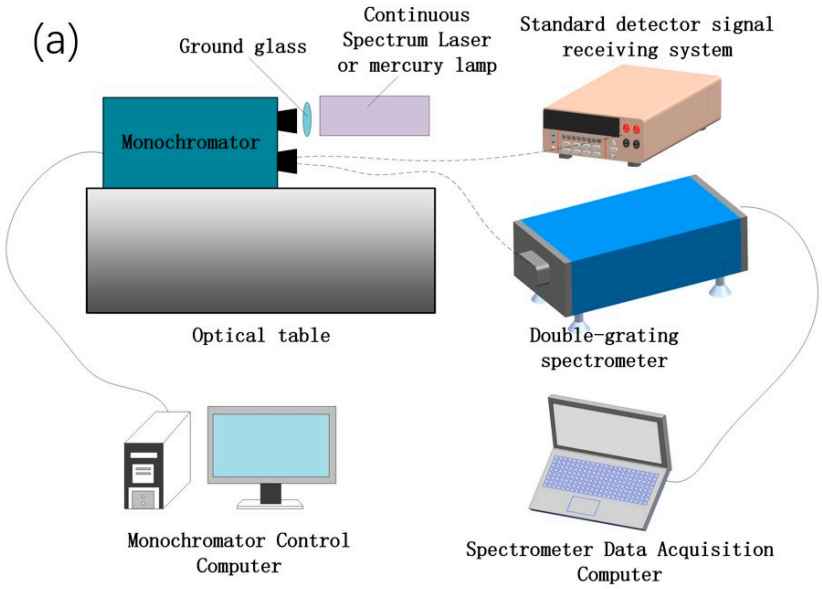

Figure 16. *Cont.*

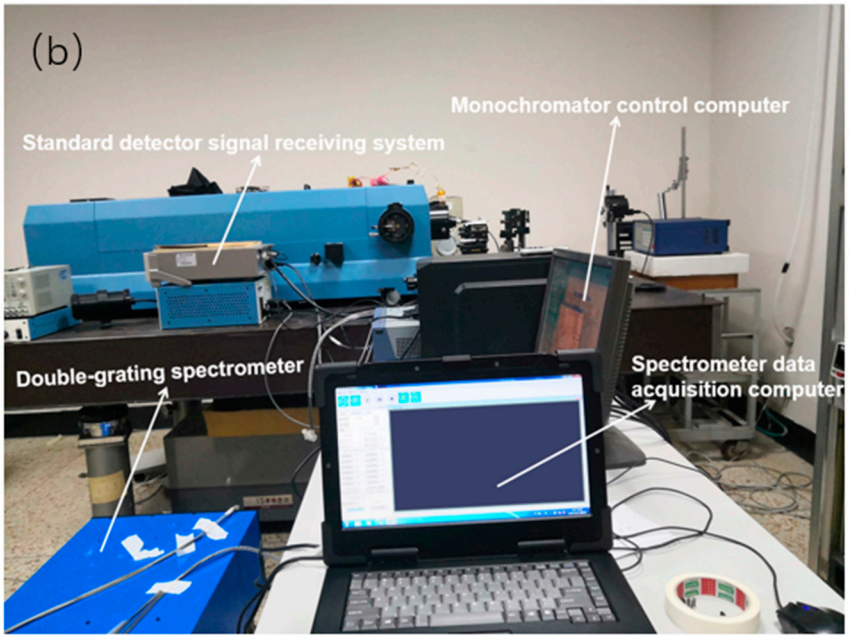

Figure 16. Water vapor absorption band (758–880 nm) spectrum calibration system: (**a**) Water vapor absorption band (758–880 nm) spectrum calibration flow chart; (**b**) The instrument of the water vapor absorption band (758–880 nm) spectrum calibration system and the working principle.

For the calibration of the molecular oxygen A-band observation channels, 10 scanning bands were selected with a scan interval of 0.004 nm. For the calibration of the water vapor absorption band observation channel, six scanning bands were selected with a scan interval of 0.025 nm. Each band takes 51 sets of data to ensure that the spectral response function of several PBSCs can be drawn. Some of the spectral response functions calibrated for the molecular oxygen A-band observation channel (channel 1, 2, 3) and the water vapor absorption band observation channel (channel 4, 5, 6) are shown in Figure 17, and the data results are listed in Tables 2–7.

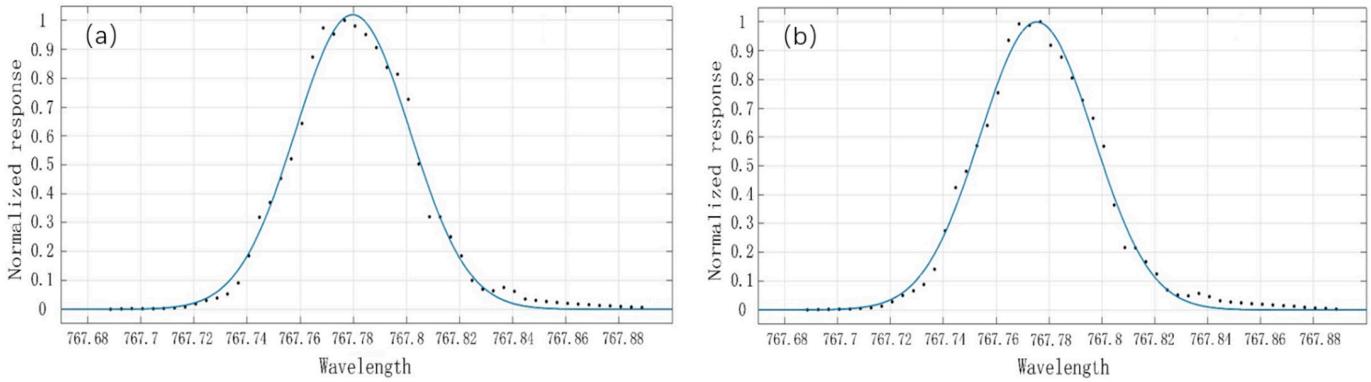

Figure 17. *Cont.*

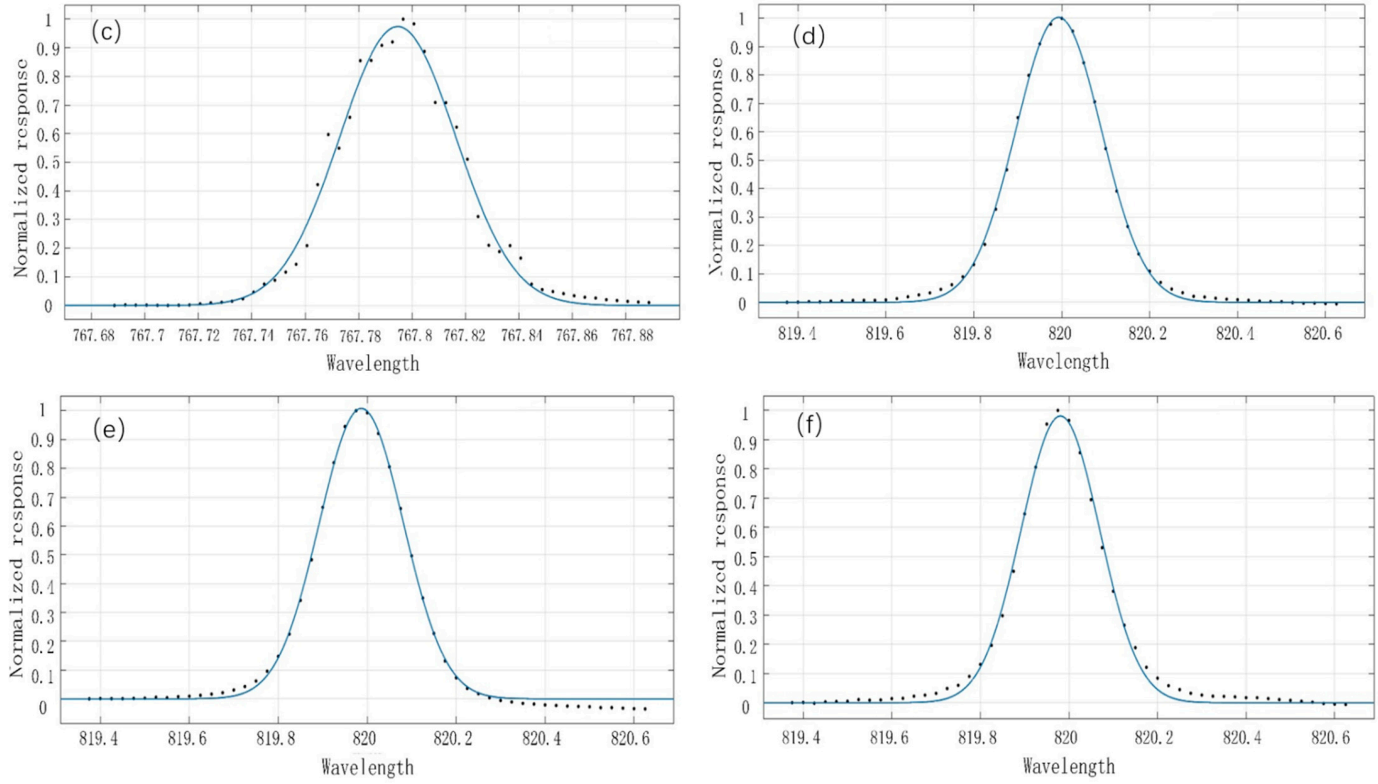

Figure 17. Spectral response function diagram of some PBSCs of molecular oxygen A-band (1, 2, 3 channels) and water vapor absorption band (4, 5, 6 channels): (**a**) Channel 1, 977 PBSC spectral response function (Center wavelength: 767.7798 nm, Full-Width Half-Maximum: <0.050 nm, R^2 = 0.9904, RMSE = 0.03501); (**b**) Channel 2, 977 PBSC spectral response function (Center wavelength: 767.7754 nm, Full-Width Half-Maximum: <0.050 nm, R^2 = 0.9922, RMSE = 0.03094); (**c**) Channel 3, 991 PBSC spectral response function (Center wavelength: 767.7946 nm, Full-Width Half-Maximum: <0.055 nm, R^2 = 0.9870, RMSE = 0.03913); (**d**) Channel 4, 1030 PBSC spectral response function (Center wavelength: 819.993 nm, Full-Width Half-Maximum: <0.23 nm, R^2 = 0.9988, RMSE = 0.01108); (**e**) Channel 5, 1025 PBSC spectral response function (Center wavelength: 819.987 nm, Full-Width Half-Maximum: <0.23 nm, R^2 = 0.9976, RMSE = 0.01613); (**f**) Channel 6, 1020 PBSC spectral response function (Center wavelength: 819.981 nm, Full-Width Half-Maximum: <0.21 nm, R^2 = 0.9952, RMSE = 0.02045).

Table 2. Spectral calibration results of molecular oxygen A-band with observation channel (channel 1).

PBSC Number	Center Wavelength (nm)	Full-Width Half-Maximum (nm)
199	757.7952	0.05
354	759.7906	0.05
510	761.7984	0.05
665	763.7869	0.055
822	765.7961	0.05
978	767.7923	0.05
1135	769.7962	0.055
1292	771.7943	0.05
1449	773.7945	0.055
1606	775.7881	0.05

Table 3. Spectral calibration results of molecular oxygen A-band with observation channel (channel 2).

PBSC Number	Center Wavelength (nm)	Full-Width Half-Maximum (nm)
205	757.8034	0.055
360	759.7987	0.05
515	761.7939	0.05
671	763.7953	0.05
827	765.7913	0.05
977	767.7754	0.05
1140	769.7919	0.05
1297	771.7896	0.055
1454	773.7900	0.05
1612	775.7963	0.05

Table 4. Spectral calibration results of molecular oxygen A-band with observation channel (channel 3).

PBSC Number	Center Wavelength (nm)	Full-Width Half-Maximum (nm)
212	757.7962	0.05
367	759.7935	0.05
523	761.7999	0.05
679	763.8009	0.05
835	765.7977	0.05
991	767.7942	0.055
1148	769.7979	0.055
1305	771.7887	0.055
1461	773.7838	0.055
1619	775.7907	0.055

Table 5. Spectral calibration results of water vapor absorption band with observation channel (channel 4).

PBSC Number	Center Wavelength (nm)	Full-Width Half-Maximum (nm)
13	757.975	0.2
449	784.595	0.2
833	808.006	0.2
1227	831.9901	0.2
1622	856.010	0.2
2017	880.013	0.21

Table 6. Spectral calibration results of water vapor absorption band with observation channel (channel 5).

PBSC Number	Center Wavelength (nm)	Full-Width Half-Maximum (nm)
9	758.005	0.2
444	784.566	0.21
829	808.031	0.21
1223	832.002	0.2
1618	856.012	0.21
2013	880.003	0.21

Table 7. Spectral calibration results of water vapor absorption band with observation channel (channel 6).

PBSC Number	Center Wavelength (nm)	Full-Width Half-Maximum (nm)
11	758.367	0.2
440	784.571	0.21
824	807.98	0.2
1219	832.010	0.21
1614	856.011	0.21
2009	879.997	0.22

After the center wavelengths of the above-mentioned several PBSCs were obtained, the data can be fitted to obtain the center wavelengths of each PBSC [54,55]. Polynomial fitting was performed on the above data, and 1- to 4-order polynomial models were, respectively, taken for processing. The results are listed in Tables 8–13. In the fitting results, y represents the center wavelength, and x represents the spectral line channel number.

Table 8. Fitting results of the corresponding relationship between the center wavelength of the molecular oxygen A-band observation channel (channel 1) and the PBSC.

Fitting Order	Fitting Result	Standard Deviation (nm)	R^2
First-order	$y = 0.001278x + 756.0849$	0.01788	1
Second-order	$y = -6.71 \times 10^{-8} \cdot x^2 + 0.001290x + 756.0456$	0.00417	1
Third-order	$y = 1.49 \times 10^{-11} \cdot x^3 - 1.09 \times 10^{-8} \cdot x^2 + 0.001293x + 756.0403$	0.00397	1
Fourth-order	$y = 4.93 \times 10^{-14} \cdot x^4 + 1.49 \times 10^{-11} \cdot x^3 - 1.09 \times 10^{-8} \cdot x^2 + 0.001293x + 756.0403$	0.00356	1

Table 9. Fitting results of the corresponding relationship between the center wavelength of the molecular oxygen A-band observation channel (channel 2) and the PBSC.

Fitting Order	Fitting Result	Standard Deviation (nm)	R^2
First-order	$y = 0.001278x + 756.1036$	0.02228	0.999
Second-order	$y = -8.46 \times 10^{-8} \cdot x^2 + 0.001294x + 756.0542$	0.00417	1
Third-order	$y = 1.28 \times 10^{-11} \cdot x^3 - 1.20 \times 10^{-8} \cdot x^2 + 0.001297x + 756.0498$	0.00396	1
Fourth-order	$y = 2.99 \times 10^{-14} \cdot x^4 - 9.86 \times 10^{-11} \cdot x^3 + 1.54 \times 10^{-8} \cdot x^2 + 0.001291x + 756.0565$	0.00392	1

Table 10. Fitting results of the corresponding relationship between the center wavelength of the molecular oxygen A-band observation channel (channel 3) and the PBSC.

Fitting Order	Fitting Result	Standard Deviation (nm)	R^2
First-order	$y = 0.001278x + 756.0838$	0.01458	1
Second-order	$y = -5.50 \times 10^{-8} \cdot x^2 + 0.001290x + 756.0517$	0.00326	1
Third-order	$y = -3.13 \times 10^{-11} \cdot x^3 - 4.63 \times 10^{-8} \cdot x^2 + 0.001289x + 756.0528$	0.00335	1
Fourth-order	$y = -2.02 \times 10^{-14} \cdot x^4 + 7.22 \times 10^{-11} \cdot x^3 - 1.38 \times 10^{-8} \cdot x^2 + 0.001293x + 756.0482$	0.00337	1

Table 11. Fitting results of the corresponding relationship between the center wavelength of the water vapor absorption band observation channel (channel 4) and the PBSC.

Fitting Order	Fitting Result	Standard Deviation (nm)	R^2
First-order	$y = 0.006089x + 757.2379$	0.04043	1
Second-order	$y = -9.40 \times 10^{-8} \cdot x^2 + 0.06108x + 757.1841$	0.00470	1
Third-order	$y = 1.64 \times 10^{-11} \cdot x^3 - 1.44 \times 10^{-8} \cdot x^2 + 0.06112x + 757.1806$	0.00284	1
Fourth-order	$y = 5.32 \times 10^{-15} \cdot x^4 - 5.28 \times 10^{-12} \cdot x^3 - 1.17 \times 10^{-7} \cdot x^2 + 0.06111x + 757.1809$	0.00289	1

Table 12. Fitting results of the corresponding relationship between the center wavelength of the water vapor absorption band observation channel (channel 5) and the PBSC.

Fitting Order	Fitting Result	Standard Deviation (nm)	R^2
First-order	$y = 0.06087x + 757.5170$	0.04548	1
Second-order	$y = -1.05 \times 10^{-7} \cdot x^2 + 0.06109x + 757.4534$	0.00701	1
Third-order	$y = 2.89 \times 10^{-11} \cdot x^3 - 1.93 \times 10^{-7} \cdot x^2 + 0.06115x + 757.4517$	0.00204	1
Fourth-order	$y = 2.38 \times 10^{-15} \cdot x^4 + 1.92 \times 10^{-11} \cdot x^3 - 1.81 \times 10^{-7} \cdot x^2 + 0.06115x + 757.4477$	0.00210	1

Table 13. Fitting results of the corresponding relationship between the center wavelength of the water vapor absorption band observation channel (channel 6) and the PBSC.

Fitting Order	Fitting Result	Standard Deviation (nm)	R^2
First-order	$y = 0.06087x + 757.7645$	0.04954	1
Second-order	$y = -1.16 \times 10^{-7} \cdot x^2 + 0.06110x + 757.6994$	0.00729	1
Third-order	$y = 2.59 \times 10^{-11} \cdot x^3 - 1.94 \times 10^{-7} \cdot x^2 + 0.06116x + 757.6940$	0.00431	1
Fourth-order	$y = 1.59 \times 10^{-14} \cdot x^4 - 3.86 \times 10^{-11} \cdot x^3 - 1.13 \times 10^{-7} \cdot x^2 + 0.06113x + 757.6949$	0.00413	1

As mentioned above, with the increase in the fitting order, the accuracy of fitting the relationship between the center wavelength and the PBSC is continuously improving. The use of second-order polynomials for fitting significantly affects the reduction in the standard deviation in the fitting. After the third-order fitting is applied, the fitting standard deviations in the channels are all less than 0.004 nm (molecular oxygen A-band) and 0.005 nm (water vapor absorption band). Meanwhile, with the increase in the fitting order, the coefficients of the newly added higher-order terms are continuously decreasing. When the fourth-order fitting is applied, the standard deviation in the fitting does not decrease significantly, and the coefficient of determination R^2 remains at 1. It indicates that the third-order polynomial fitting can obtain a better fitting result, and it is not necessary to use a higher-order polynomial for fitting.

After spectral calibration, the results of optical-mechanical design and adjustment were verified. The measured spectral resolutions of DGSS 1, 2, and 3 channels were all better than 0.07 nm (0.06 nm), and the 4, 5, and 6 channels were better than 0.28 nm (0.24 nm). The observation band of DGSS covers the molecular oxygen A-band (758–778 nm) and the water vapor band (758–880 nm), thus meeting the needs.

3.1.2. Radiometric Calibration

For the radiometric calibration of DGSS, it is necessary to select a suitable calibration light source. The measurement uncertainty of the bidirectional reflectance distribution function of the diffuse reflector is large (4~6%) when using the spectral irradiance standard lamp and the diffuse reflector for calibration, and the spectral radiance cannot be adjusted during the calibration process. Furthermore, other traditional spectral radiance standard light sources, e.g., high-temperature black body or tungsten strip lamps, are too small to fill the field of view of the instrument, and the instrument will receive radiation from other light sources in the environment. After analysis and discussion, a spectroradiometer and a standard lamp are used to transfer the aperture radiance standard of the integrating sphere, and then the integrating sphere is used as the standard light source to calibrate the DGSS. In this way, the light emitted by the standard light source that fills the field of view of the instrument and the calibration result with a lower uncertainty can be obtained.

The calibration was carried out using a Sphereoptics TX-20Z-UV integrating sphere system with a diameter of 500 mm and an opening diameter of 203.2 mm. The inner wall coating of the integrating sphere is Zenith material with strong UV radiation resistance and good cosine characteristics. The 150 W halogen tungsten light source and 300 W xenon light source are installed on it, and the stability is 0.5%/h after the light source is lit for half an hour. A silicon detector is installed on the wall of the integrating sphere to detect the size and stability of the signal inside the sphere. According to its linear response, the light flux of the light source into the integrating sphere is controlled by adjusting the width of the slit, and the spectral radiance of the output of the integrating sphere is controlled to achieve radiometric calibration of the instrument. The entire calibration process was performed in a dark room, with one channel opened and the other five channels closed at a time. The placement of the instrument before the test is shown in Figure 18.

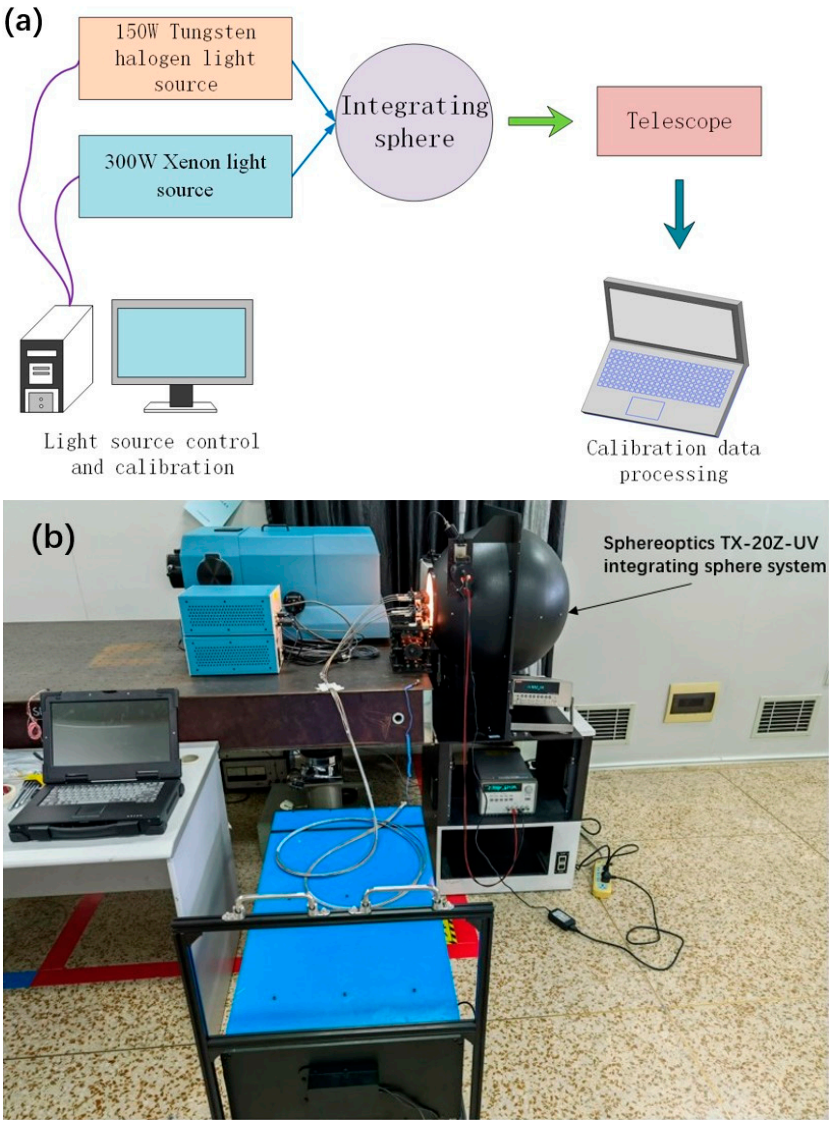

Figure 18. (**a**) Schematic of the radiance calibration of the instrument; (**b**) Instrument placement during radiation calibration evaluation.

The exposure time of the detector selected by DGSS can be adjusted arbitrarily between 0.2–10,900 ms. To observe under different weather and solar radiance conditions, the exposure time of the detector also needs to be adjusted during operation. In this way, when the instrument works under different integration times and different radiances, there is a problem with the mutual conversion of readings. According to the field test results, the exposure time of the detector needs to be adjusted between 1000–1500 ms when it is working normally. Therefore, it is necessary to understand the relationship between the detector responses under different integration times to analyze the relationship between the detector responses and the radiance under different integration times. During the radiometric calibration, the integrated time linearity and radiance linearity analysis data can be collected and directly analyzed.

Figure 19 shows the fitting results of the linear radiance response of the 1024th PBSC of six channels. The original data points are all near the fitting curve, $R^2 = 1$, with good linearity. Similar results were obtained in the analysis of several PBSCs.

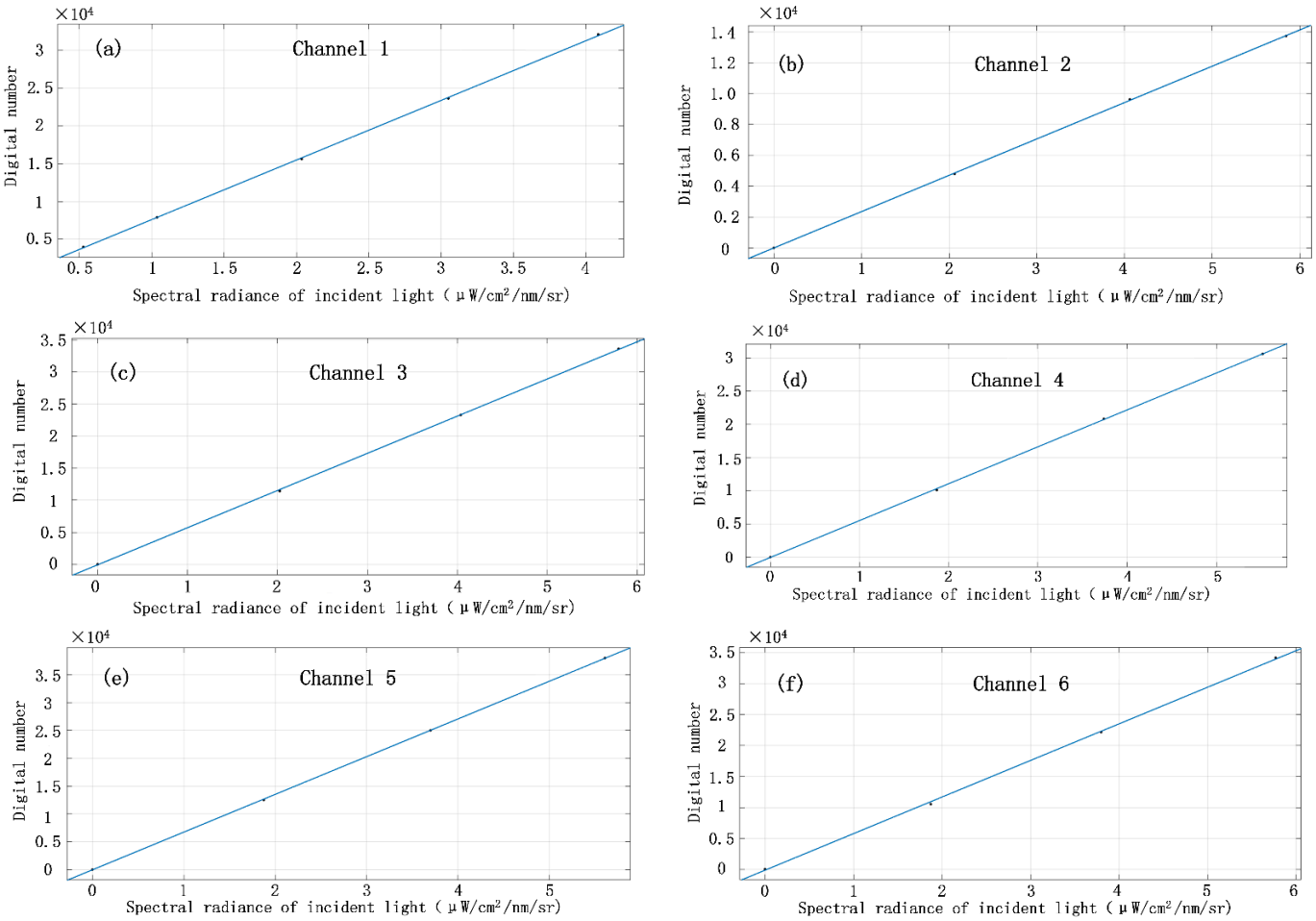

Figure 19. Fitting results of the linear radiance response of the 1024 PBSC for the six channels: (**a**) Channel 1; (**b**) Channel 2; (**c**) Channel 3; (**d**) Channel 4; (**e**) Channel 5; (**f**) Channel 6.

Figure 20 shows the fitting results of the linear integrated time response of the 1024th PBSC of six channels. The original data points are all near the fitting curve, $R^2 = 1$, with good linearity. Similar results were obtained in the analysis of several spectral channels.

Therefore, the DGSS has a good linear response under the variation in the integration time and the input radiance. The relationship between the data of different radiances collected with different integration times in different situations and the calibration data can be directly calculated.

The SNR test is conducted in a dark room surrounded by a black cloth. The test process is as follows. First, open the integrating sphere, preheat for 30 min, fix the lens barrel on the support, adjust the position of the support to ensure that the lens barrel is aligned with the opening center of the integrating sphere, turn on the detector, simulate the actual detection of low-radiance targets by adjusting the spectral brightness output by the integrating sphere, and record multiple groups of detection conditions by DGSS.

According to Equation (10) in Section 2.1.2, the SNR of each channel for a low-radiance target can be calculated, as shown in Figure 21. The two dimensions on the plane coordinate are the spatial dimension pixel number and the spectral dimension pixel number, and the vertical axis is the SNR corresponding to the pixel. Therefore, the SNR of a single pixel is low (<40), which is difficult to meet the observation requirements (>100).

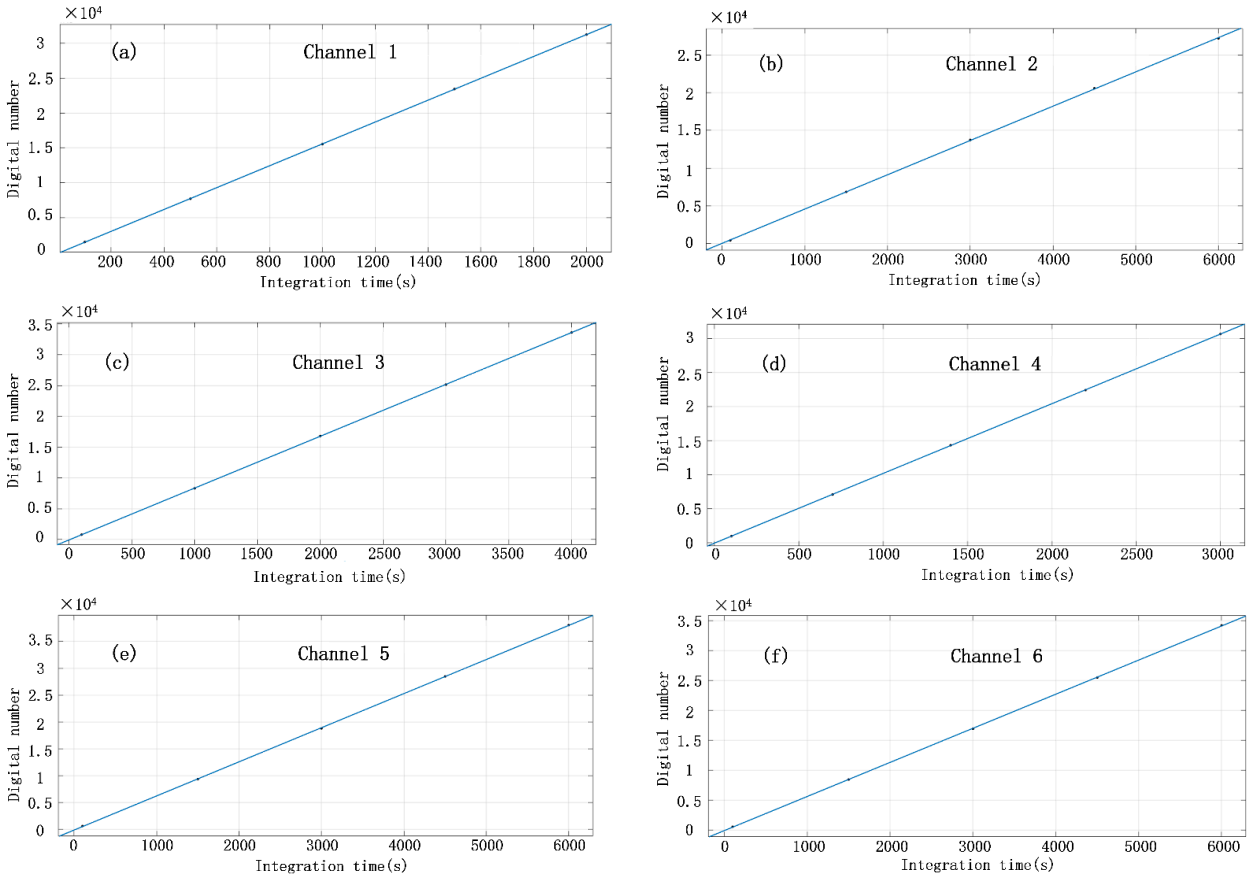

Figure 20. Fitting results of the linear integrated time response of the 1024 PBSC for the six channels: (**a**) Channel 1; (**b**) Channel 2; (**c**) Channel 3; (**d**) Channel 4; (**e**) Channel 5; (**f**) Channel 6.

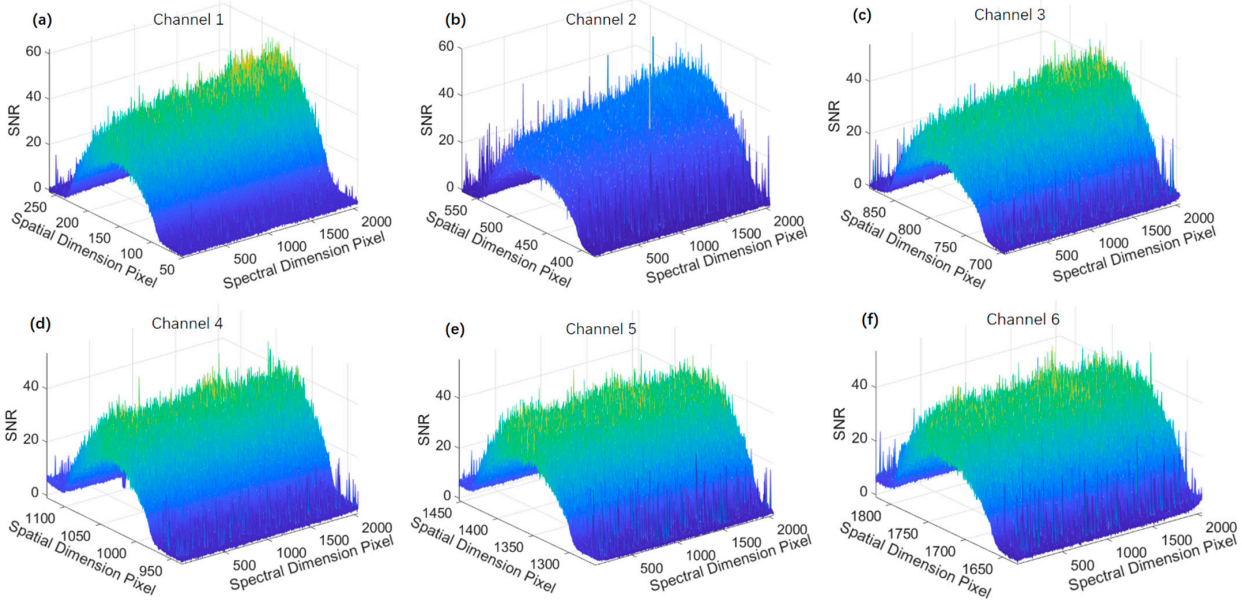

Figure 21. SNR of a single pixel (**a**) Channel 1; (**b**) Channel 2; (**c**) Channel 3; (**d**) Channel 4; (**e**) Channel 5; (**f**) Channel 6.

Generally, the SNR is improved by reducing noise or enhancing the signal. For DGSS, stray light suppression and detector refrigeration have been adopted to reduce the system noise, but some inherent noises such as quantization noise and shot noise cannot

be eliminated. For the method of improving the signal, the slit size is determined by the optical design, and the energy entering the system is also determined. Therefore, pixel combination in the spatial dimension is usually used to improve the SNR. The calculation results of SNR after pixel combination in the spatial dimension are shown in Figure 22. The probability density distribution of SNR after pixel combination in the spatial dimension is shown in Figure 23. It can be seen that the SNR has been greatly improved (>100), meeting the design and use indicators.

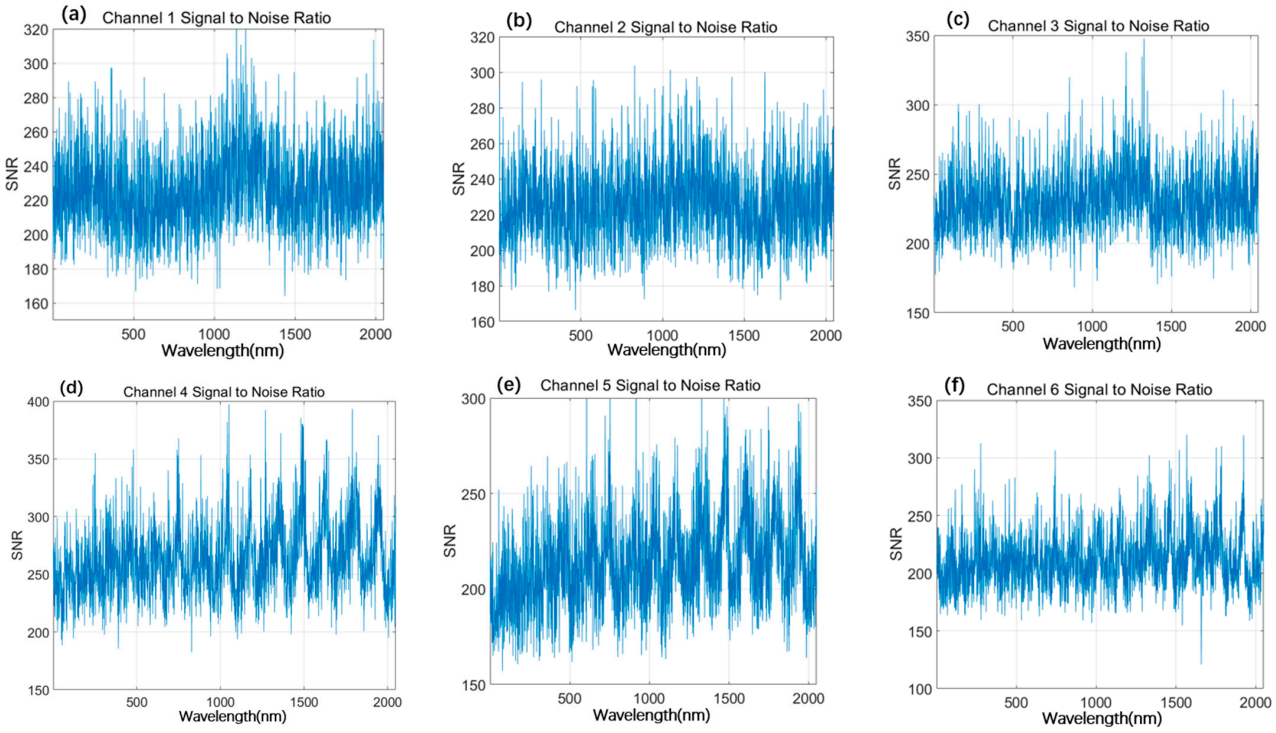

Figure 22. SNR after spatial dimension pixel combination(**a**) Channel 1; (**b**) Channel 2; (**c**) Channel 3; (**d**) Channel 4; (**e**) Channel 5; (**f**) Channel 6.

According to the output signal of DGSS illuminated by integrating sphere light source and the spectral radiance of integrating sphere light source, the radiation response of DGSS on each channel can be calculated. To be consistent with the field observation conditions, the area of the radiation source should be larger than the optical entrance pupil area of DGSS, and the whole aperture angle should be illuminated at the same time. During the radiation response experiment, each channel needs to be tested separately, as shown in Figure 24.

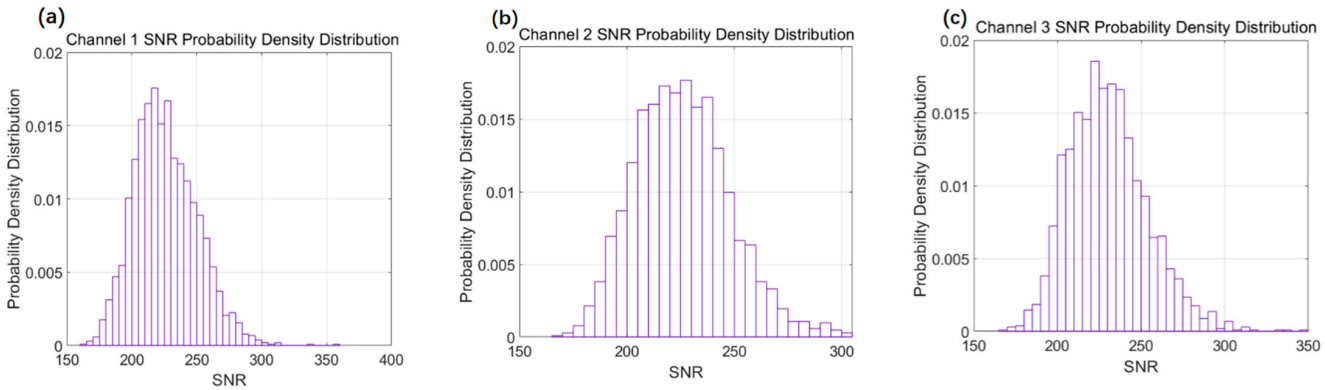

Figure 23. *Cont.*

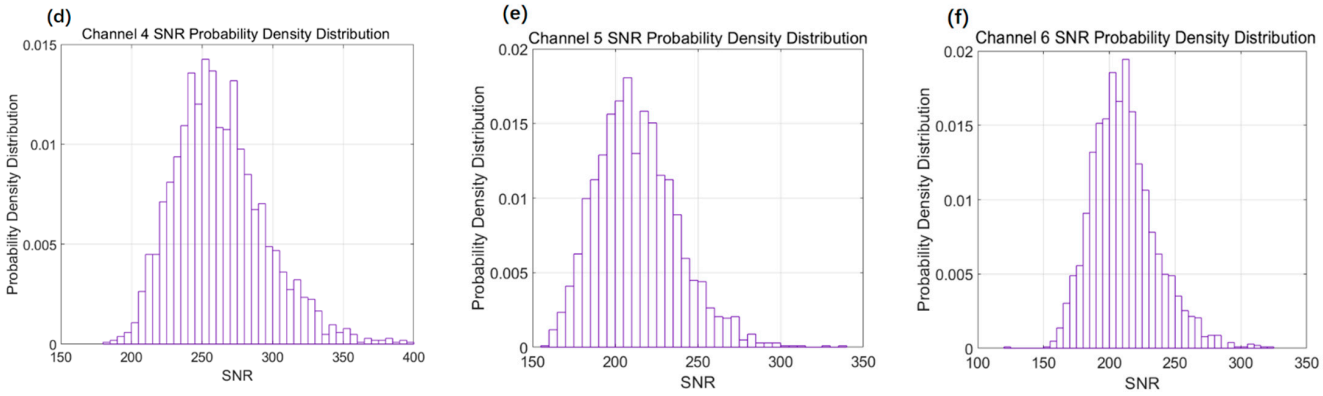

Figure 23. Probability density distribution of SNR after spatial pixel combination (**a**) Channel 1; (**b**) Channel 2; (**c**) Channel 3; (**d**) Channel 4; (**e**) Channel 5; (**f**) Channel 6.

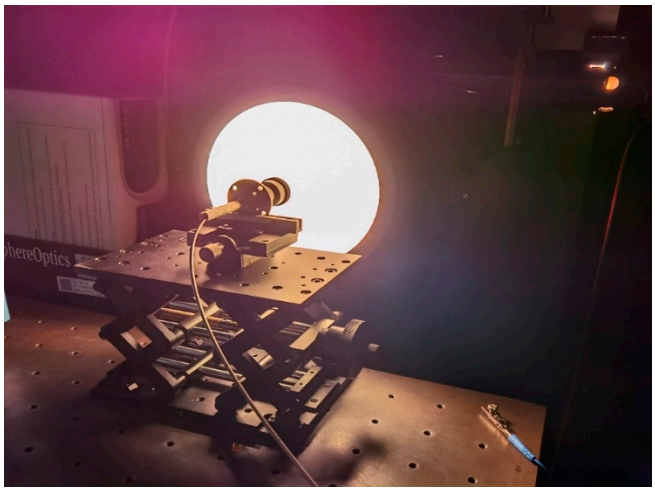

Figure 24. Placement of the telescope and integrating sphere light source during radiation response test.

In the field observation, the signal value received by the direct channel is much larger than that received by the scattering channel. Similarly, the signal value of the channel with a large angle in the scattering channel will also be smaller than that of the channel with a small angle. Since the light from different angles shares the same detector, it is necessary to place a suitable neutral density filter at the front end of the channel with a large signal value. The neutral density filter is not installed during the radiation response test, and the transmittance of the neutral density filter is tested separately with the lambda 950 spectrophotometer. The fitting curve between the radiation response test results in the laboratory and the transmittance test results of the filter (consistent with the field test state) is shown in Figure 25. The fluctuation of the fitting curve is caused by the influence of the interference fringes mentioned in Section 2.2.1. When the calibration conditions are consistent with the field observation conditions (including the stability of the spectral position), it can be greatly weakened.

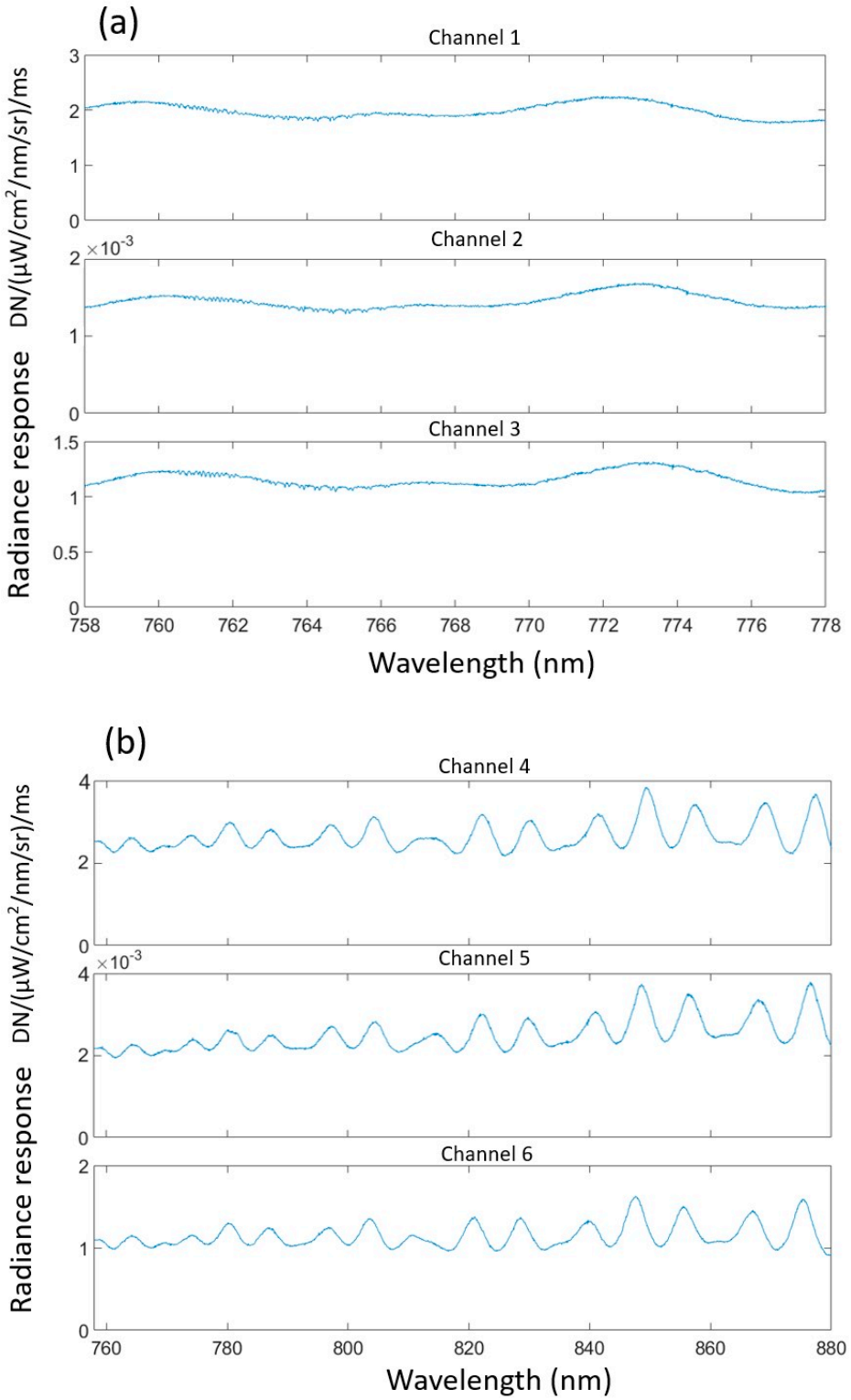

Figure 25. The fitting curve between the radiation response test results in the laboratory and the filter transmittance test results: (**a**) Molecular oxygen A-band (758–778 nm); (**b**) Water vapor absorption band (758–880 nm).

3.2. Field Measurement

After the laboratory calibration of DGSS, in order to further test its observation ability and stability, field observations were carried out under different seasons and temperature conditions. The observation site is Changchun City, Jilin Province. The daytime average

temperature in July in summer is about 28 °C, and the daytime average temperature in January in winter is about −10 °C, which basically meets most of the use conditions of the prototype. Figure 26 shows the field observation of DGSS in winter and summer. As DGSS is equipped with an air cooling device and the detector integrates a semiconductor refrigeration module; it is less affected by high temperature weather. Next, we take the low temperature situation as an example to introduce the field observation results of DGSS.

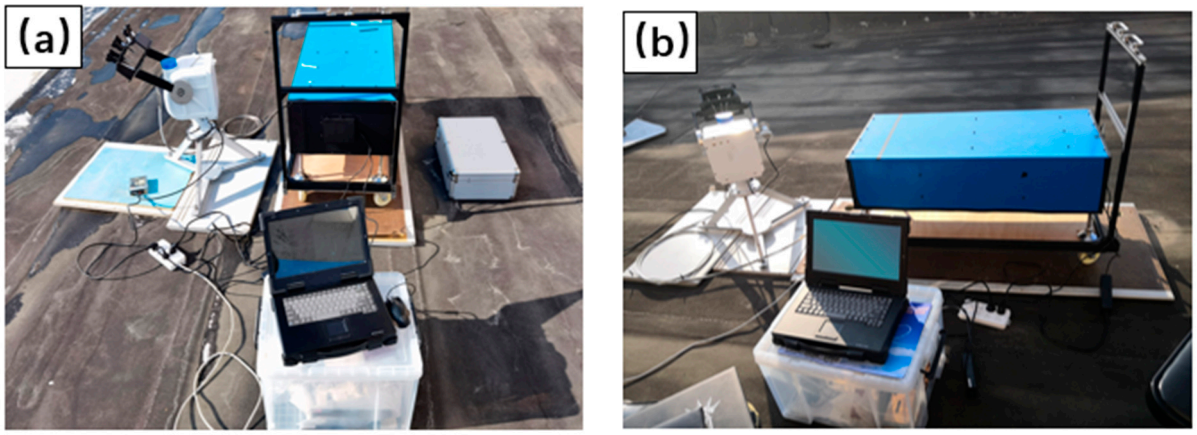

Figure 26. DGSS working outside the Changchun Observatory in Jilin Province. (**a**) In winter; (**b**) In summer.

On 29 January 2021, a field observation was conducted at the Changchun Observatory in Jilin Province to verify the observation method and the capability of DGSS. The observation station is located at 125°23′51″ east longitude and 43°50′40″ north latitude. The weather was fine that day. In the experiment, the computer, double-grating spectrometer, solar tracking turntable, and external field calibration laser were connected.

Even though the spectral drift is well controlled in the structural design, there will still be a small shift in the spectral position when the external conditions such as transportation and temperature change greatly. Thus, this study prepared a laser with stabilized center wavelength (768.587 nm) for DGSS calibration in each test. Before the field test starts, the laser is connected to the six channels of DGSS, respectively, to test the position of the laser center wavelength in the six channels. After the field test is over, each channel is retested again, and the position of the laser is used twice to correct the shift of the spectrum. The position change of the field laser before and after this test is shown in Figure 27. The total change is less than two pixels, indicating that the temperature stability of DGSS is well.

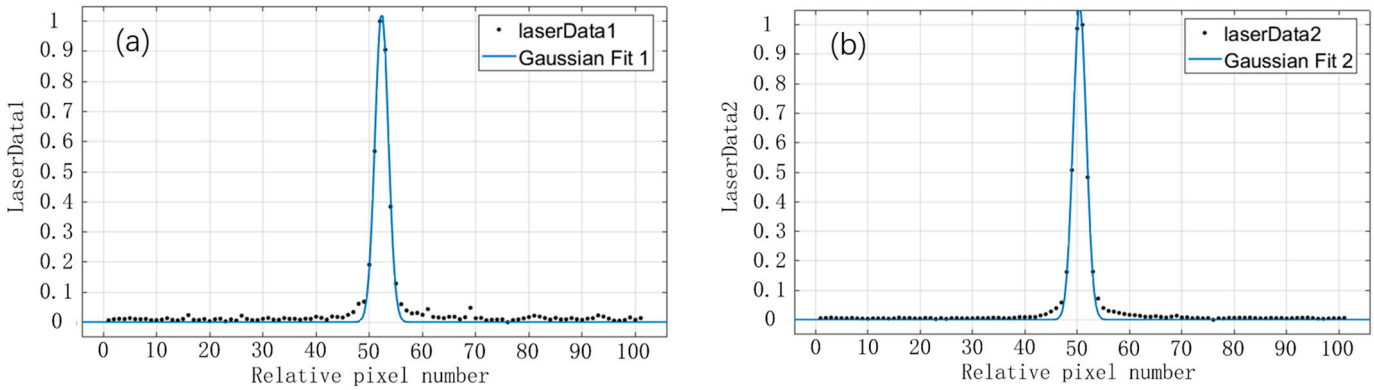

Figure 27. The position of the laser on the image plane of the detector before and after the field test: (**a**) Location before field test: 52.32; (**b**) Location after field test: 50.49.

After each channel was calibrated with the laser, the position of the turntable was adjusted to the initial state, and the turntable was controlled to track the sun. The feedback adjustment of the four-quadrant detector made the tracking accuracy within 0.1°. The acquisition software was executed to collect the sunlight data. According to the DN values of the six channels collected by the detector image plane, a neutral density filter with appropriate magnification is installed on the telescope barrel corresponding to the channel with a stronger signal. By adjusting the integration time and filter multiple times, the DN values of the six channels are at the same level, avoiding the situation where some DN values are saturated and other DN values are small. Then, DGSS enters automatic observation mode.

According to the spectral calibration, radiation calibration, and field laser test results, the curve of converting the DN value into radiance value is shown in Figure 28. The test results show that DGSS can work stably under a large temperature change and realize the basic detection function, and there is no spectral aliasing between the two bands. The absorption spectra of molecular oxygen A-band and the water vapor absorption band are preliminarily obtained.

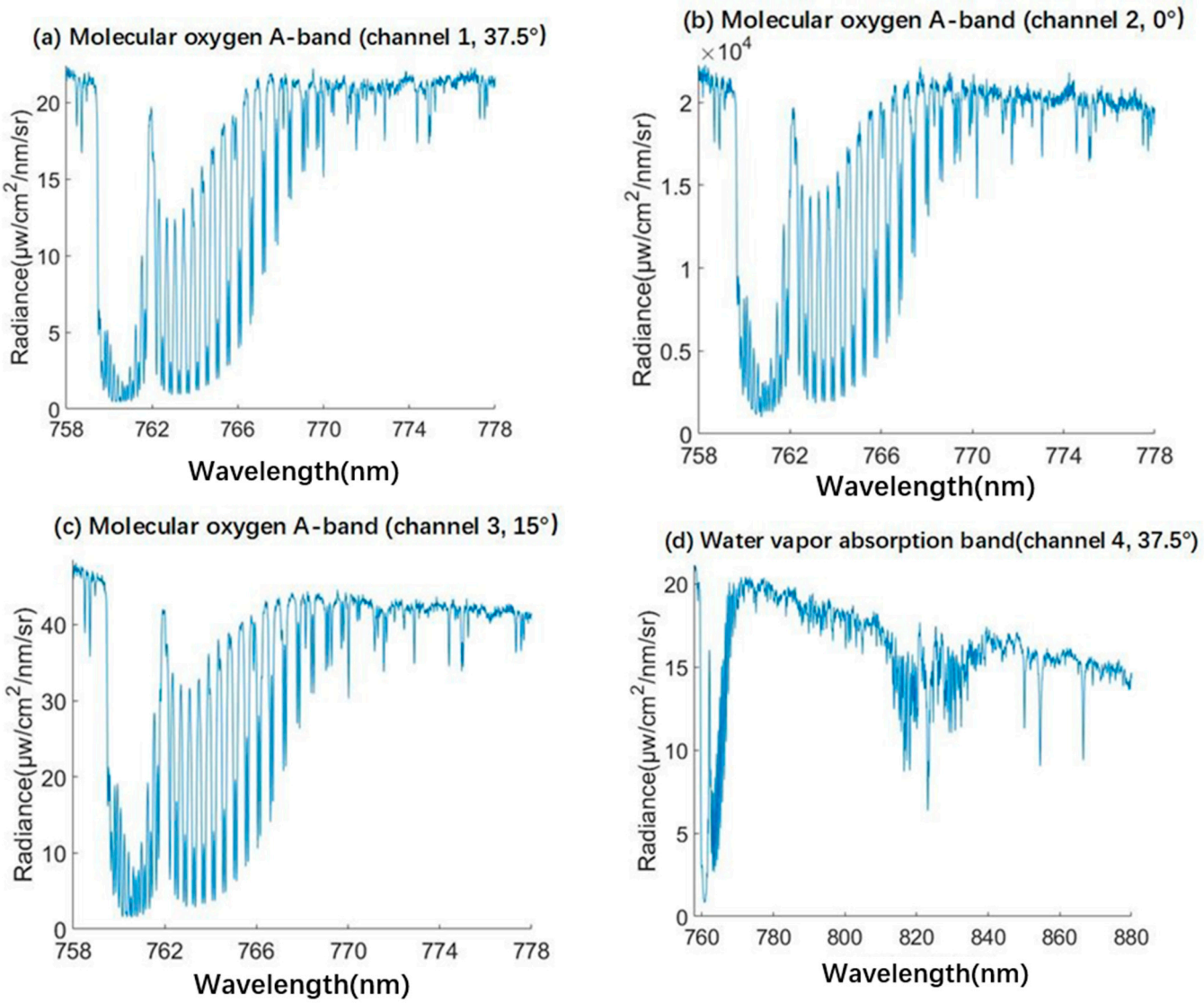

Figure 28. *Cont.*

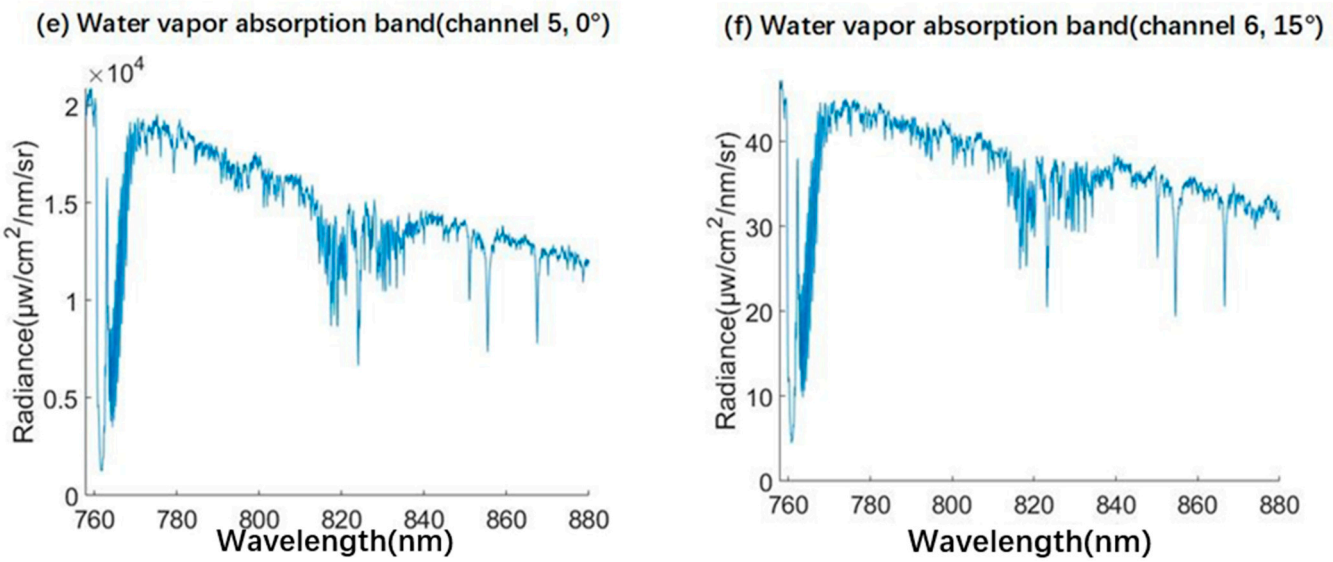

Figure 28. The diagram of converting the measured DN value of the external field in the molecular oxygen A-band (1, 2, 3 channels) and the water vapor absorption band (4, 5, 6 channels) to the radiation value.

4. Discussion

In this paper, according to the requirements of the simultaneous observation of aerosol, water vapor and cloud parameters, molecular oxygen A-band (758–778 nm), and water vapor absorption band (758–880 nm) are determined as observation bands. Then, the design, simulation, integration, calibration, and field measurement of the double-grating spectrometer system (DGSS) is conducted. Our main findings are as follows:

- Instrument performance indicators have a great influence on the observation results. It can be seen from the observation results of molecular oxygen A-band and water vapor absorption band that higher spectral resolution can help to obtain a more detailed atmospheric absorption spectrum.
- DGSS conducts three-angle observations for each waveband, and it introduces direct sunlight and sky scattered light from different angles into the spectrometer through optical fibers. Compared with single-angle observation, multi-angle observation can provide more independent variables, thereby effectively reducing inversion errors.
- If the instrument works stably and the spectral position changes little in the detector image plane under the two states of laboratory calibration and field observation, the influence of interference fringes of the back-illuminated detector in the near-infrared band can be weakened by high-precision spectral calibration and radiation calibration.
- For long-span, high-spectral resolution instruments, the deformation of the structure caused by the change of temperature and the spectral line position is obvious. DGSS has good control of the deformation through material selection and mechanical design, and the stability of DGSS to temperature change is verified by external field observations.
- When the temperature change exceeds 40 °C, the spectral position on the image plane of the detector will change to a certain extent. At this time, the instrument can be calibrated with a fixed wavelength laser before and after the experiment to determine the spectral position change. The amount of change can be corrected during subsequent data processing.
- To avoid light aliasing in the two bands (three angles in each band), it is important to ensure that the dimensions of the slit and the stop are accurate and determine their positions in the horizontal and vertical directions.
- The back-illuminated detector has low dark current and high quantum efficiency under refrigeration, which is conducive to improving the SNR. But dispersive hyperspectral

VNIR imagers using back-illuminated detectors will suffer from interference fringes in near-infrared bands.

- The multi-angle, high-resolution, and double-band simultaneous observation method of DGSS was verified. In the future, the atmosphere in different regions and different weather conditions will be observed to provide the data to atmospheric scientists. Meanwhile, inversion research will be conducted to achieve ground-based network observation after joint improvement and provide a scientific basis for human intervention and adjustment of global change trends.

5. Conclusions

This paper proposed a method for simultaneous observation of molecular oxygen A-band (758–778 nm) and water vapor absorption band (758–880 nm) from multiple aspects. Then, a double-grating spectrometer system (DGSS) was developed with spectral resolutions of 0.06 nm (758–78 nm) and 0.24 nm (758–880 nm). Finally, calibration and field observation was carried out to verify the performance of the prototype system and the feasibility of the observation method. During the design and development of DGSS, the following three problems were solved:

The first problem is the calibration of a high-resolution spectrometer, including spectral calibration and radiometric calibration. The spectral calibration of molecular oxygen A-band adopts the combination of tunable laser and wavelength meter. The spectral calibration of the water vapor absorption band adopts the combination of continuous spectrum laser and monochromator. The integrating sphere light source is selected for radiometric calibration to simulate the actual observation state. To ensure the consistency between calibration and field observation, it is necessary to overcome the influence of temperature change on the long-span spectrometer system. This problem was solved by material selection and optical system support, as described in Section 2.3.

The second problem is that multi-angle observation can provide more information for atmospheric parameters, but the signal DN values of the direct solar channel and sky scattering channel differ greatly, which will lead to direct channel saturation and small signals in other channels. In this study, several neutral density filters with different transmittance were designed to attenuate the channels with large DN values in the field observation, and the integration time was adjusted to approximate the signal values of the six channels to weaken the influence of the direct channel on the scattering channel.

The last problem is to analyze and suppress the stray light (including spectral aliasing of two bands). On the one hand, the stray light from outside the target spectral band was suppressed by installing narrow-band filters in the front optical system, and special coating treatment was also conducted on the mirrors in the system to improve the reflectivity of the target spectral band. On the other hand, the design of the size and position of the incident slit and stray light stop (as shown in Figures 11 and 12 in Section 2.2.2) prevented the spectra of the two bands from overlapping. Besides, both grating 1 and grating 2 work at level-1, and the stray light of other levels was suppressed by setting light barriers and absorption wells.

DGSS belongs to the first generation of principle prototypes to explore new observation modes. In the future, we will carry out temperature control and structural optimization of the front optical system, compare it with other remote sensing instruments, and study the correction and inversion of atmospheric parameters. In addition, we will focus on the lightweight and automation of the instrument to investigate the network layout of multiple observation stations and a wider range of remote sensing of atmospheric parameters.

Author Contributions: Conceptualization, J.L.; methodology, J.L.; software, J.L.; validation, J.L. and G.L.; formal analysis, J.L.; investigation, J.L.; resources, J.L., M.D. and G.L.; data curation, J.L.; writing—original draft preparation, J.L.; writing—review and editing, J.L., G.L., H.W., M.D., D.C. and L.W.; visualization, J.L. and H.W.; supervision, G.L.; project administration, G.L.; funding acquisition, G.L. and M.D. All authors have read and agreed to the published version of the manuscript.

Funding: This work was supported by the National Natural Science Foundation of China under Grant 41527806.

Institutional Review Board Statement: Not applicable.

Informed Consent Statement: Not Applicable.

Data Availability Statement: Data available on request.

Acknowledgments: The authors would like to thank the Changchun Observation Station for the assistance of the site and equipment.

Conflicts of Interest: The authors declare no conflict of interest.

References

1. Ramanathan, V.; Crutzen, P.J.; Kiehl, J.T.; Rosenfeld, D. Aerosols, climate, and the hydrological cycle. *Science* **2001**, *294*, 2119–2124. [CrossRef] [PubMed]
2. Kvalevåg, M.M.; Samset, B.H.; Myhre, G. Hydrological sensitivity to greenhouse gases and aerosols in a global climate model. *Geophys. Res. Lett.* **2013**, *40*, 1432–1438. [CrossRef]
3. Liu, S.; Xing, J.; Zhao, B.; Wang, J.; Wang, S.; Zhang, X.; Ding, A. Understanding of Aerosol–Climate Interactions in China: Aerosol Impacts on Solar Radiation, Temperature, Cloud, and Precipitation and Its Changes Under Future Climate and Emission Scenarios. *Curr. Pollut. Rep.* **2019**, *5*, 36–51. [CrossRef]
4. Sun, T.; Che, H.; Qi, B.; Wang, Y.; Dong, Y.; Xia, X.; Wang, H.; Gui, K.; Zheng, Y.; Zhao, H.; et al. Aerosol optical characteristics and their vertical distributions under enhanced haze pollution events: Effect of the regional transport of different aerosol types over eastern China. *Atmos. Chem. Phys.* **2018**, *18*, 2949–2971. [CrossRef]
5. Takemura, T. Simulation of climate response to aerosol direct and indirect effects with aerosol transport-radiation model. *J. Geophys. Res.* **2005**, *110*. [CrossRef]
6. Yu, X.C.; Zhi, Y.; Tang, S.J.; Li, B.B.; Gong, Q.; Qiu, C.W.; Xiao, Y.F. Optically sizing single atmospheric particulates with a 10-nm resolution using a strong evanescent field. *Light Sci. Appl.* **2018**, *7*, 18003. [CrossRef] [PubMed]
7. Bellouin, N.; Quaas, J.; Gryspeerdt, E.; Kinne, S.; Stier, P.; Watson-Parris, D.; Boucher, O.; Carslaw, K.S.; Christensen, M.; Daniau, A.L.; et al. Bounding Global Aerosol Radiative Forcing of Climate Change. *Rev. Geophys.* **2020**, *58*, e2019RG000660. [CrossRef]
8. Mishra, A.K.; Koren, I.; Rudich, Y. Effect of aerosol vertical distribution on aerosol-radiation interaction: A theoretical prospect. *Heliyon* **2015**, *1*, e00036. [CrossRef]
9. Reid, J.S.; Kuehn, R.E.; Holz, R.E.; Eloranta, E.W.; Kaku, K.C.; Kuang, S.; Newchurch, M.J.; Thompson, A.M.; Trepte, C.R.; Zhang, J.; et al. Ground-based High Spectral Resolution Lidar observation of aerosol vertical distribution in the summertime Southeast United States. *J. Geophys. Res. Atmos.* **2017**, *122*, 2970–3004. [CrossRef]
10. Pan, Z.; Mao, F.; Wang, W.; Zhu, B.; Lu, X.; Gong, W. Impacts of 3D Aerosol, Cloud, and Water Vapor Variations on the Recent Brightening during the South Asian Monsoon Season. *Remote Sens.* **2018**, *10*, 651. [CrossRef]
11. Feng, H.; Zou, B. Satellite-based estimation of the aerosol forcing contribution to the global land surface temperature in the recent decade. *Remote Sens Environ.* **2019**, *232*, 111299. [CrossRef]
12. Suzuki, K.; Takemura, T. Perturbations to Global Energy Budget Due to Absorbing and Scattering Aerosols. *J. Geophys. Res. Atmos.* **2019**, *124*, 2194–2209. [CrossRef]
13. Alizadeh-Choobari, O.; Gharaylou, M. Aerosol impacts on radiative and microphysical properties of clouds and precipitation formation. *Atmos. Res.* **2017**, *185*, 53–64. [CrossRef]
14. Seinfeld, J.H.; Bretherton, C.; Carslaw, K.S.; Coe, H.; DeMott, P.J.; Dunlea, E.J.; Feingold, G.; Ghan, S.; Guenther, A.B.; Kahn, R.; et al. Improving our fundamental understanding of the role of aerosol-cloud interactions in the climate system. *Proc. Natl. Acad. Sci. USA* **2016**, *113*, 5781–5790. [CrossRef]
15. Waquet, F.; Cornet, C.; Deuzé, J.L.; Dubovik, O.; Ducos, F.; Goloub, P.; Herman, M.; Lapyonok, T.; Labonnote, L.C.; Riedi, J.; et al. Retrieval of aerosol microphysical and optical properties above liquid clouds from POLDER/PARASOL polarization measurements. *Atmos. Meas. Tech.* **2013**, *6*, 991–1016. [CrossRef]
16. Cheng, F.; Zhang, J.; He, J.; Zha, Y.; Li, Q.; Li, Y. Analysis of aerosol-cloud-precipitation interactions based on MODIS data. *Adv. Space Res.* **2017**, *59*, 63–73. [CrossRef]
17. Zeng, Z.-C.; Chen, S.; Natraj, V.; Le, T.; Xu, F.; Merrelli, A.; Crisp, D.; Sander, S.P.; Yung, Y.L. Constraining the vertical distribution of coastal dust aerosol using OCO-2 O_2 A-band measurements. *Remote Sens. Environ.* **2020**, *236*, 111494. [CrossRef]
18. Xie, H.; Zhou, T.; Fu, Q.; Huang, J.; Huang, Z.; Bi, J.; Shi, J.; Zhang, B.; Ge, J. Automated detection of cloud and aerosol features with SACOL micro-pulse lidar in northwest China. *Opt. Express* **2017**, *25*, 30732–30753. [CrossRef]
19. Katkovsky, L.; Martinov, A.; Siliuk, V.; Ivanov, D.; Kokhanovsky, A. Fast Atmospheric Correction Method for Hyperspectral Data. *Remote Sens.* **2018**, *10*, 1698. [CrossRef]
20. Wu, S.; Song, X.; Liu, B.; Dai, G.; Liu, J.; Zhang, K.; Qin, S.; Hua, D.; Gao, F.; Liu, L. Mobile multi-wavelength polarization Raman lidar for water vapor, cloud and aerosol measurement. *Opt. Express* **2015**, *23*, 33870–33892. [CrossRef]

21. Bian, Y.; Zhao, C.; Xu, W.; Kuang, Y.; Tao, J.; Wei, W.; Ma, N.; Zhao, G.; Lian, S.; Tan, W.; et al. A novel method to retrieve the nocturnal boundary layer structure based on CCD laser aerosol detection system measurements. *Remote Sens. Environ.* **2018**, *211*, 38–47. [CrossRef]
22. Allan, R.P.; Barlow, M.; Byrne, M.P.; Cherchi, A.; Douville, H.; Fowler, H.J.; Gan, T.Y.; Pendergrass, A.G.; Rosenfeld, D.; Swann, A.L.S.; et al. Advances in understanding large-scale responses of the water cycle to climate change. *Ann. N. Y. Acad. Sci.* **2020**, *1472*, 49–75. [CrossRef] [PubMed]
23. Zhou, F.-C.; Song, X.; Leng, P.; Wu, H.; Tang, B.-H. An Algorithm for Retrieving Precipitable Water Vapor over Land Based on Passive Microwave Satellite Data. *Adv. Meteorol.* **2016**, *2016*, 1–11. [CrossRef]
24. Knopf, D.A.; Alpert, P.A.; Wang, B. The Role of Organic Aerosol in Atmospheric Ice Nucleation: A Review. *ACS Earth Space Chem.* **2018**, *2*, 168–202. [CrossRef]
25. Tretyakov, M.Y. Spectroscopy underlying microwave remote sensing of atmospheric water vapor. *J. Mol. Spectrosc.* **2016**, *328*, 7–26. [CrossRef]
26. Gui, K.; Che, H.; Chen, Q.; Zeng, Z.; Zheng, Y.; Long, Q.; Sun, T.; Liu, X.; Wang, Y.; Liao, T.; et al. Water vapor variation and the effect of aerosols in China. *Atmos. Environ.* **2017**, *165*, 322–335. [CrossRef]
27. Lin, P.; Paynter, D.; Ming, Y.; Ramaswamy, V. Changes of the Tropical Tropopause Layer under Global Warming. *J. Clim.* **2017**, *30*, 1245–1258. [CrossRef]
28. Spinhirne, J.D.; Palm, S.P.; Hart, W.D.; Hlavka, D.L.; Welton, E.J. Cloud and aerosol measurements from GLAS: Overview and initial results. *Geophys. Res. Lett.* **2005**, *32*. [CrossRef]
29. Dai, A.; Rasmussen, R.M.; Liu, C.; Ikeda, K.; Prein, A.F. A new mechanism for warm-season precipitation response to global warming based on convection-permitting simulations. *Clim Dynam.* **2017**, *55*, 343–368. [CrossRef]
30. Vaquero-Martínez, J.; Antón, M.; Sanchez-Lorenzo, A.; Cachorro, V.E. Evaluation of Water Vapor Radiative Effects Using GPS Data Series over Southwestern Europe. *Remote Sens.* **2020**, *12*, 1307. [CrossRef]
31. Lu, C.W.; Fu, J.; Liu, X.F.; Chen, W.W.; Hao, J.L.; Li, X.L.; Pant, O.P. Air pollution and meteorological conditions significantly contribute to the worsening of allergic conjunctivitis: A regional 20-city, 5-year study in Northeast China. *Light Sci. Appl.* **2021**, *10*, 190. [CrossRef] [PubMed]
32. Liu, M.; Vecchi, G.A.; Smith, J.A.; Knutson, T.R. Causes of large projected increases in hurricane precipitation rates with global warming. *npj Clim. Atmos. Sci.* **2019**, *2*, 38. [CrossRef]
33. Suzuki, K.; Stephens, G.L.; Golaz, J.-C. Significance of aerosol radiative effect in energy balance control on global precipitation change. *Atmos. Sci. Lett.* **2017**, *18*, 389–395. [CrossRef]
34. Fan, J.; Wang, Y.; Rosenfeld, D.; Liu, X. Review of Aerosol–Cloud Interactions: Mechanisms, Significance, and Challenges. *J. Atmos. Sci.* **2016**, *73*, 4221–4252. [CrossRef]
35. Vasilchenko, S.; Mikhailenko, S.N.; Campargue, A. Water vapor absorption in the region of the oxygen A-band near 760 nm. *J. Quant. Spectrosc. Radiat. Transfer* **2021**, *275*, 107847. [CrossRef]
36. Min, Q.; Yin, B.; Li, S.; Berndt, J.; Harrison, L.; Joseph, E.; Duan, M.; Kiedron, P. A high-resolution oxygen A-band spectrometer (HABS) and its radiation closure. *Atmos. Meas. Tech.* **2014**, *7*, 1711–1722. [CrossRef]
37. Colosimo, S.F.; Natraj, V.; Sander, S.P.; Stutz, J. A sensitivity study on the retrieval of aerosol vertical profiles using the oxygen A-band. *Atmos. Meas. Tech.* **2016**, *9*, 1889–1905. [CrossRef]
38. Geddes, A.; Bösch, H. Tropospheric aerosol profile information from high-resolution oxygen A-band measurements from space. *Atmos. Meas. Tech.* **2015**, *8*, 859–874. [CrossRef]
39. Nanda, S.; Veefkind, J.P.; de Graaf, M.; Sneep, M.; Stammes, P.; de Haan, J.F.; Sanders, A.F.J.; Apituley, A.; Tuinder, O.; Levelt, P.F. A weighted least squares approach to retrieve aerosol layer height over bright surfaces applied to GOME-2 measurements of the oxygen A band for forest fire cases over Europe. *Atmos. Meas. Tech.* **2018**, *11*, 3263–3280. [CrossRef]
40. Chang, X.; Bian, L.; Zhang, J. Large-scale phase retrieval. *eLight* **2021**, *1*, 4. [CrossRef]
41. Pelletier, B.; Frouin, R.J.; Frouin, R.; Andrefouet, S.; Kawamura, H.; Dubuisson, P.; Lynch, M.J.; Pan, D.; Platt, T. Retrieval of the aerosol vertical distribution from atmospheric radiance. In Proceedings of the Remote Sensing of Inland, Coastal and Oceanic Waters, Noumea, New Caledonia, 18–21 November 2008.
42. Hollstein, A.; Fischer, J. Retrieving aerosol height from the oxygen A band: A fast forward operator and sensitivity study concerning spectral resolution, instrumental noise, and surface inhomogeneity. *Atmos. Meas. Tech.* **2014**, *7*, 1429–1441. [CrossRef]
43. Zeng, Z.C.; Natraj, V.; Xu, F.; Pongetti, T.J.; Shia, R.L.; Kort, E.A.; Toon, G.C.; Sander, S.P.; Yung, Y.L. Constraining Aerosol Vertical Profile in the Boundary Layer Using Hyperspectral Measurements of Oxygen Absorption. *Geophys. Res. Lett.* **2018**, *45*, 10772–10780. [CrossRef]
44. Lee, R.A.M.; O'Dell, C.W.; Wunch, D.; Roehl, C.M.; Osterman, G.B.; Blavier, J.-F.; Rosenberg, R.; Chapsky, L.; Frankenberg, C.; Hunyadi-Lay, S.L.; et al. Preflight Spectral Calibration of the Orbiting Carbon Observatory 2. *IEEE Trans. Geosci. Remote Sens.* **2017**, *55*, 2499–2508. [CrossRef]
45. Wu, C.; Qi, C.; Hu, X.; Gu, M.; Yang, T.; Xu, H.; Lee, L.; Yang, Z.; Zhang, P. FY-3D HIRAS Radiometric Calibration and Accuracy Assessment. *IEEE Trans. Geosci. Remote Sens.* **2020**, *58*, 3965–3976. [CrossRef]
46. Frankenberg, C.; Hasekamp, O.; O'Dell, C.; Sanghavi, S.; Butz, A.; Worden, J. Aerosol information content analysis of multi-angle high spectral resolution measurements and its benefit for high accuracy greenhouse gas retrievals. *Atmos. Meas. Tech.* **2012**, *5*, 1809–1821. [CrossRef]

47. Chen, X.; Xu, X.; Wang, J.; Diner, D.J. Can multi-angular polarimetric measurements in the oxygen-A and B bands improve the retrieval of aerosol vertical distribution? *J. Quant. Spectrosc. Radiat. Transfer* **2021**, *270*, 107679. [CrossRef]
48. Hasekamp, O.P. Capability of multi-viewing-angle photo-polarimetric measurements for the simultaneous retrieval of aerosol and cloud properties. *Atmos. Meas. Tech.* **2010**, *3*, 839–851. [CrossRef]
49. Merlin, G.; Riedi, J.; Labonnote, L.C.; Cornet, C.; Davis, A.B.; Dubuisson, P.; Desmons, M.; Ferlay, N.; Parol, F. Cloud information content analysis of multi-angular measurements in the oxygen A-band: Application to 3MI and MSPI. *Atmos. Meas. Tech.* **2016**, *9*, 4977–4995. [CrossRef]
50. Hu, B.; Sun, D.; Liu, Y. A Novel Method to Remove Fringes for Dispersive Hyperspectral VNIR Imagers Using Back-Illuminated CCDs. *Remote Sens.* **2018**, *10*, 79. [CrossRef]
51. Xue, Q.; Lu, F.; Duan, M.; Zheng, Y.; Wang, X.; Cao, D.; Lin, G.; Tian, J. Optical design of double-grating and double wave band spectrometers using a common CCD. *Appl. Opt.* **2018**, *57*, 6823–6830. [CrossRef]
52. Kang, M.; Ahn, M.-H.; Liu, X.; Jeong, U.; Kim, J. Spectral Calibration Algorithm for the Geostationary Environment Monitoring Spectrometer (GEMS). *Remote Sens.* **2020**, *12*, 2846. [CrossRef]
53. Druy, M.A.; Crocombe, R.A.; Bannon, D.P.; Ziph-Schatzberg, L.; Woodman, P.; Nakanishi, K.; Cornell, J.; Wiggins, R.; Swartz, B.; Holasek, R. Compact, high performance hyperspectral systems design and applications. In Proceedings of the Next-Generation Spectroscopic Technologies VIII, Baltimore, MD, USA, 20–22 April 2015.
54. Sun, C.; Wang, M.; Cui, J.; Yao, X.; Chen, J. Comparison and analysis of wavelength calibration methods for prism–Grating imaging spectrometer. *Results Phys.* **2019**, *12*, 143–146. [CrossRef]
55. Martimort, P.; Kimura, T.; Neeck, S.P.; He, W.; Li, C.; Zhou, C.; Ma, L.; Zhao, Y. A smile effect correction method for dispersive imaging spectrometer based on simultaneous radiometric and spectral calibration. In Proceedings of the Sensors, Systems and Next-Generation Satellites XXII, Berlin, Germany, 10–12 September 2018.